ICARUS **127,** 461–484 (1997)
ARTICLE NO. IS975704

The Three-Dimensional Structure of the Zodiacal Dust Bands

William T. Reach

Universities Space Research Association and NASA Goddard Space Flight Center, Code 685, Greenbelt, Maryland 20771, and Institut d'Astrophysique Spatiale, Bâtiment 121, Université Paris XI, 91405 Orsay Cedex, France
E-mail: reach@ias.fr

Bryan A. Franz

General Sciences Corporation, NASA Goddard Space Flight Center, Code 970.1, Greenbelt, Maryland 20771

and

Janet L. Weiland

Hughes STX, NASA Goddard Space Flight Center, Code 685.9, Greenbelt, Maryland 20771

Received July 18, 1996; revised January 2, 1997

Using observations of the infrared sky brightness by the Cosmic Background Explorer (COBE)[1] Diffuse Infrared Background Experiment (DIRBE) and Infrared Astronomical Satellite (IRAS), we have created maps of the surface brightness Fourier-filtered to suppress the smallest (< 1°) structures and the large-scale background (>15°). Dust bands associated with the Themis, Koronis, and Eos families are readily evident. A dust band associated with the Maria family is also present. The parallactic distances to the emitting regions of the Koronis, Eos, and Maria dust bands were found to be 1.4 to 2.5 AU. A weak dust band associated with the Eunomia/Io family is evident, together with another weak and previously unattributed dust band, which may split further into two band pairs, potentially associated with the Hygiea or Vesta family. The brightnesses of the blended Themis/Koronis bands and the Eos dust band vary with ecliptic longitude, such that the northern or southern component of the band pair becomes brighter when its tilt brings it into the ecliptic plane. We attribute the brightness variations to the motion of the Earth within the emitting region, and conclude that at least some dust-band particles are on Earth-crossing orbits. For the Themis and Koronis families, the tilt is sufficient that the Earth may pass to the edges of the emitting region, where the density is highest, leading to "glints" two or four times a year. We compared the observed distributions to theoretically motivated, empirical models for the three-dimensional distribution of asteroid family dust. In the torus model, the dust is distributed among the asteroid family members with the same distributions of proper orbital inclination and semimajor axis but a random ascending node. In the migrating model, particles are presumed to be under the influence of Poynting–Robertson drag, so that they are distributed throughout the inner Solar System. The migrating model is better able to match the parallactic variation of dust-band latitude as well as the 12- to 60-μm spectrum of the dust bands. The annual brightness variations can be explained only by the migrating model. Upper limits are placed on the dust density associated with the Nysa and Flora families—both of the large, inner-belt families with wide inclination dispersions. The association of five (and potentially seven) dust bands with the largest asteroid families suggests that dust bands are an integral part of asteroid families. If nonfamily asteroids produce dust at a rate similar to that of the families with the lowest dust density, then they can account for the brightness of the zodiacal light in the ecliptic.

I. INTRODUCTION

The interplanetary dust bands, first discovered in observations by the Infrared Astronomy Satellite (IRAS) (Low *et al.* 1984, Hauser *et al.* 1984), provide a link between an asteroidal source of interplanetary dust and the present cloud that now fills the inner Solar System and produces the zodiacal light. A similar link for a cometary source of meteoroids is provided by the discovery, also in the IRAS data, of narrow dust trails, first in the orbit of P/Tempel 2 (Davies *et al.* 1984, Sykes *et al.* 1986) and then, in a systematic survey, in the orbits several other periodic comets (Sykes and Walker 1992). These discoveries made it

[1] The National Aeronautics and Space Administration/Goddard Space Flight Center (NASA/GSFC) is responsible for the design, development, and operation of the Cosmic Background Explorer (COBE). Scientific guidance is provided by the COBE Science Working Group. GSFC is also responsible for the development of the analysis software and for the production of the mission data sets.

0019-1035/97 $25.00

possible to directly observe the regions where interplanetary dust is produced, and now we hope to trace the connection between its source and its present distribution. This connection is difficult because the dust bands and trails are low-surface-brightness enhancements on the very bright and relatively smooth zodiacal light.

In this paper we study the asteroidal dust bands using new observations and theoretical calculations. Based on the fact that the dust bands come in pairs with peak latitudes comparable to the largest concentrations of asteroids, they were quickly associated with the Hirayama (1918) asteroid families (Dermott *et al.* 1984). A dust band can form as the consequence of the catastrophic disruption of a main-belt asteroid: the shattered fragments disperse and comminute to produce a long-lived, edge-brightened torus of dust (Sykes and Greenberg 1986, Sykes *et al.* 1989). The Poynting–Robertson lifetimes of the small particles that probably produce the observed infrared emission are smaller than the time it takes to form a band pair, so these particles are spread from the asteroid belt throughout the inner Solar System (Reach 1992). The asteroid families themselves may be the result of a primordial disruption of a large parent asteroid, after which the fragments comminute to the present distribution (Chapman *et al.* 1989, Marzari *et al.* 1995). Because the dust bands are associated with asteroid families, their observed properties, including their existence or nonexistence for each asteroid family, reveal unique information about the evolution of the asteroids.

The new observations of the infrared sky brightness are those of the Diffuse Infrared Background Experiment (DIRBE) aboard the Cosmic Background Explorer (COBE) satellite (Boggess *et al.* 1992). The improved calibration and rapid, redundant sky coverage make the DIRBE observations more suited than the earlier IRAS observations for studying the time-variable emission from the Solar System, and the wider range of wavelengths has already allowed the first detection of the dust bands in scattered light (Spiesman *et al.* 1995). The observing strategy for DIRBE was designed to modulate the Solar System emission because it is the dominant source of sky brightness and therefore must be accurately removed before any conclusions can be drawn about the cosmic background radiation, which was the primary goal of the COBE mission. The investigation described here was partially motivated by the need to understand the structure of the interplanetary dust cloud as part of the effort to model the diffuse infrared emission from the Solar System.

Our approach is to determine the distribution of dust responsible for the observed dust bands. To this end, we compare empirical models for the dust distribution to the observed surface brightness, both having been processed similarly. A different and complementary approach has been taken by the group at the University of Florida (cf. Dermott *et al.* 1996), who use the physical forces (solar gravity and radiation pressure, and Poynting–Robertson and solar wind drag) known to influence dust particles to simulate the evolution of particles of asteroidal origin. This approach has the advantage of being implicitly self-consistent and physical, taking the dust from ''source to sink.'' It has also led to the discovery of the Earth's resonant dust ring (Dermott *et al.* 1994b); however, the dynamical approach is only as accurate as the assumptions built into its initial conditions and the physical forces that are assumed to operate on the dust. In a previous paper (Reach 1992) and more completely in the present paper, it was shown that previous models for the distribution of dust responsible for the dust bands (Dermott *et al.* 1985, Sykes and Greenberg 1986) were incorrect, having neglected a physical force that in fact dominates their distribution. More recent numerical simulations including the Poynting–Robertson effect confirm its dominant influence on the evolution of dust particles (Dermott *et al.* 1994a). In light of the large number of assumptions required for the numerical simulations to be tractable, and the wide range of possible initial conditions for the dust, we have preferred to use physically motivated but empirical formulas for the dust density as a function of position. The three-dimensional models can be tuned to match the observations, from which we learn what is the true distribution of interplanetary dust.

II. OBSERVATIONS AND DATA REDUCTION

A. DIRBE Zodiacal Light Maps

We created a set of zodiacal light maps using the weekly sky maps from the DIRBE dataset. The combination of the orbit of the COBE satellite (in which DIRBE resides) and the rotation of the field of view about the satellite spin axis allows DIRBE to completely map half of the sky in 1 week. To improve signal-to-noise and minimize the effect of non-Solar System contributions to the sky brightness, we combined weekly maps into monthly zodiacal light maps as follows. Diffuse galactic emission from the interstellar medium and unresolved starlight were subtracted from each weekly map using estimates of their brightness in all wavebands (Hauser 1996). The diffuse starlight was subtracted using a model that reproduces the number-magnitude counts of a wide range of galactic infrared sources (Wainscoat *et al.* 1992). The interstellar medium was subtracted by correlating the 100-μm map with 21-cm line observations of the H I column density, and then by correlating each DIRBE waveband with the scaled 100-μm template (Weiland *et al.* 1996). All pixels containing point sources were masked. Then four consecutive weekly maps were rotated such that the Sun is in the center, and the overlapping unmasked pixels were combined. We combined the values for a given pixel by interpolating their

brightness to a time corresponding to the middle of the month. Thus the entire map is referred to a fixed time, which is important for reducing the variations due to small changes in the position of the Sun from one observation to another. The maps have a much-reduced contamination from galactic emission, as well as being relatively free of point sources. This latter effect is due to the fact that fixed point sources move from week to week in our corotating coordinate system; a pixel that is masked for one week does not affect the average for the monthly map.

As a complement to the monthly zodiacal light maps, which are effectively "snapshots" of the variation of brightness with latitude and solar elongation, we used the observations tangent to the Earth's orbit, i.e., at a solar elongation of 90° leading or trailing the Earth, to create all-sky zodiacal light maps. The diffuse emission of the Galaxy was removed as described above. Separate maps were created for observations leading and trailing the Earth. The DIRBE elongation-90 maps have less integration time per unit area than the IRAS HCON 1 and 2 maps, because the DIRBE field of view was rotating about the spacecraft orbital axis, effectively spreading the integration time over the 60°-wide viewing swath. What the DIRBE observations lack in sensitivity, however, is made up for by the improved photometric stability and redundancy of coverage. The fluctuations in the IRAS maps at the spatial frequencies of interest here are dominated by calibration drifts between successive orbits, rather than true detector noise. A given longitude, observed 90° elongation leading the Earth, was reobserved trailing the Earth 6 months later. Thus, comparing the leading and trailing elongation-90 maps allows us to observe both the true temporal variation of the observed brightness and seasonal effects due to the motion of the Earth in its orbit. The COBE mission lasted 41 weeks, so the leading (or trailing) map covers some 79% of the ecliptic. The gaps in the leading and trailing maps do not overlap, so the region with overlapping coverage is 58% of the ecliptic.

B. Locating the Zodiacal Dust Bands

The dust bands are low-contrast features in the zodiacal light, and they appear in pairs approximately symmetrically located with respect to the ecliptic. High-pass filtering allows the bands to be seen easily in our monthly zodiacal light maps, with a signal-to-noise comparable to that obtained with the IRAS data (cf. Sykes 1988). In order to quantitatively measure the locations and brightnesses of the dust bands, we have edited the Fourier transforms of the surface brightness as a function ecliptic latitude. First, a profile I, from either the elongation-90° map or the monthly skymap, was Fourier transformed into $\mathscr{F}(I)$. Second, a smoothed version was created by taking the inverse transform

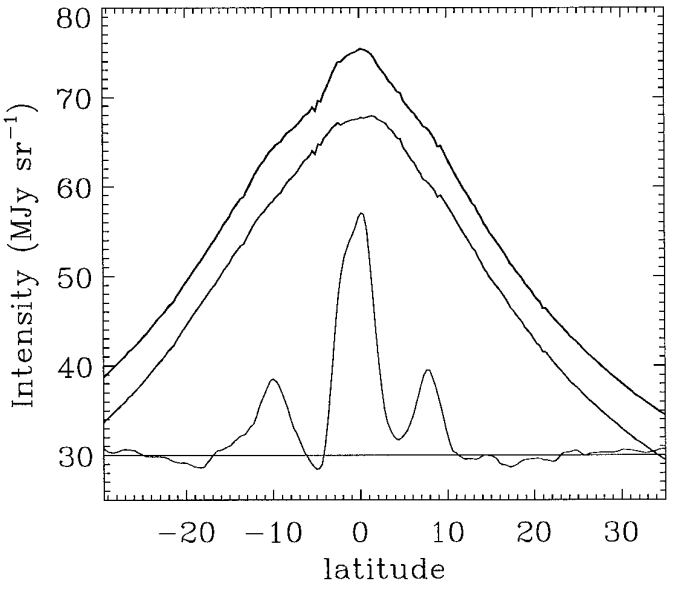

FIG. 1. Surface brightness profile of the ecliptic from a COBE DIRBE 25-μm waveband monthly zodiacal light map. The upper, thick curve shows the total surface brightness, I. The lower curve shows the filtered profile, I_f, obtained with the Fourier method described in the text, emphasizing structures with vertical angular size between 3° and 15°. It has been scaled by a factor of 10 and shifted for clarity; the plotted quantity is $10I_f + 30$. The middle curve is the difference $I - I_f$, shifted vertically for clarity because it is so nearly equal to I; the plotted quantity is $I - I_f - 5$.

$$I_s = \mathscr{F}^{-1}[\mathscr{F}(I)e^{-f^2/2f_s^2}],$$

where f is the spatial frequency; this effectively isolates the low spatial frequencies in the profile without introducing high-frequency ringing. Third, a noise-suppressed profile was created with the inverse transform

$$I' = \mathscr{F}^{-1}[\mathscr{F}(I)(1 - e^{-f^4/f_N^4})];$$

this effectively suppressed the high spatial frequencies. The filtered profile was then created as

$$I_f = I' - I_s.$$

This technique enhances structures with angular scales in the range $f_s^{-1} < \theta < f_N^{-1}$. We found that the outer (±10° and ±17°) dust bands are sufficiently broad to require $f_s^{-1} \simeq 15°$, while they benefit from a low noise level with $f_N^{-1} \simeq 3°$. The inner dust bands are narrower; they require both a flatter background, obtained by setting $f_s^{-1} \simeq 7°$, and a higher resolution, obtained by setting $f_N^{-1} \simeq 1°$. An example of a latitude profile, I, filtered profile, I_f, and the difference between these profiles is shown in Fig. 1. It is evident that nearly all of the structure has been extracted from the original profile, and no traces of the dust bands

are evident in the difference profile. Maps of the filtered brightness for 25-μm observations in February 1990 in the direction leading the Earth are shown in Fig. 2, both for the larger-scale dust bands (a) and in more detail near the ecliptic for the smaller-scale dust bands (b). Finally, the filtered elongation-90 maps leading and trailing the Earth are shown in Fig. 3.

The dust bands at $\pm 10°$ and $\pm$ 1.4° are prominent in the filtered maps. Further, an additional band pair at $\pm 17°$ appears in the larger-scale map, and substructure in the $\pm 1.4°$ band appears in the smaller-scale map. The full widths at half-maximum brightness of the northern and southern components of the $\pm 10°$ dust band are around 3.5°, whereas those of the $\pm 1.4°$ dust band are around 1.5°. These widths are the same as found by a Gaussian and polynomial decomposition of the total (unfiltered) surface brightness (Reach 1992), and are not related to the lower spatial-frequency cutoff of the Fourier filter; however, it is very likely that a smooth part of the dust-band emission has been removed by the filtration process. Very extended emission related to the dust bands has been noted before (Reach 1992, Jones and Rowan-Robinson 1993). Looking ahead to the results of the dust-band models that we derive in this work (Fig. 16), there is very extended emission from the dust bands at high ecliptic latitudes. In this work we consider the structured part of the surface brightness because it contains the clear signature of the dust bands; therefore, we will have to apply the same Fourier filtering to any models to be compared to the data.

To measure the latitudes precisely, we fitted vertical slices from each map with several Gaussians. While the Gaussian shape is not theoretically motivated, it is a convenient fitting function and is able to reproduce the filtered profiles adequately. For the wide-scale monthly maps (e.g., Fig. 2), a minimum of 3 Gaussians was required (one for the marginally resolved $\pm 1.4°$ band pair and one each for the northern and southern components of the $\pm 10°$ band pair), but a significantly better fit was achieved with a 6-Gaussian fit (2 each for the $\pm 1.4°$, $\pm 10°$, and $\pm 17°$ band pairs). The improvement of the χ^2 goodness-of-fit for a particular slice as the number of Gaussians increases is shown in Table I. A further improvement in goodness-of-fit was achieved by an 8-Gaussian fit to this slice. The additional Gaussians correspond to a splitting of the $\pm 10°$ band pair into two; the additional band pair has a latitude $\pm 7°$. This additional apparent band pair, however, does not persist at all elongations and is not well detected; we will conservatively neglect it for now. Slices from the smaller-scale monthly maps (Fig. 2b) are well fitted by a combination of 4 Gaussians, 2 each for the $\pm 1.4°$ and $\pm 10°$ band pairs.

Images similar to those shown in Fig. 2 were generated for each of 10 months, for leading and trailing observations, for the 25- and 60-μm wavebands (a total of 40 maps). These images were used to determine the variation of the band location and parallax with time of year. For the wider-scale monthly maps, a 3-Gaussian fit was performed at each longitude, while for the smaller-scale monthly maps, a 4-Gaussian fit was performed. For the two months (February and July) with best separation between the ecliptic and galactic planes, we created maps in the other 8 wavebands (an additional 32 maps). These images were used to determine the location and brightness of the dust bands at different wavelengths.

C. Parallax of the Dust Bands

The perceived separation between northern and southern components of a band pair increases as a function of solar elongation, because the distance from the Earth to the emitting region decreases. The separations for the band pairs are shown in Fig. 4. Four sets of points are shown in (a) and (b), corresponding to the 25- and 60-μm observations, leading and trailing the Sun. The separation for the $\pm 17°$ band pair, shown in (c), was measured for only one image. The parallactic widening of the band-pair separation with increasing solar elongation is clear for all three band pairs. The solid curves in Fig. 4 are fits of a simple ''ring-pair'' model (described below) to the parallactic variation of separation with elongation.

D. Tilt of the Dust Bands

The latitudes of the dust bands vary as a function of observation date as well as solar elongation. This effect is easily seen as the smooth, sinusoidal longitude variation of the northern and southern components of each band pair in the elongation-90 maps (Fig. 3), as well as the change in the centroid of the dust bands from monthly map to monthly map. In Fig. 5, the annual variation of the average of northern and southern component latitude is shown. Points were obtained from the elongation-90 maps as well as the monthly zodiacal light maps (where the portion between 80° and 100° was used). There is a clear trend of the centroid as a function of heliocentric longitude, which we interpret as being due to the tilt of the centroid of the emitting region with respect to the ecliptic. The solid curves are sinusoidal fits, which are used below to define the ''ring-pair'' model of the dust bands. The locations where the midplane of a dust band crosses the ecliptic plane can be determined graphically from this diagram (Dermott *et al.* 1988): they correspond to the dates when observations leading and trailing the Earth have equal and opposite geocentric ecliptic latitudes. The locations of the ascending and descending nodes are shown in Fig. 5 as dashed lines. It is noteworthy that both the ascending node (at 86 $\pm$ 3° for the $\pm 1.4°$ bands and at 92 $\pm$ 4° for the $\pm 10°$

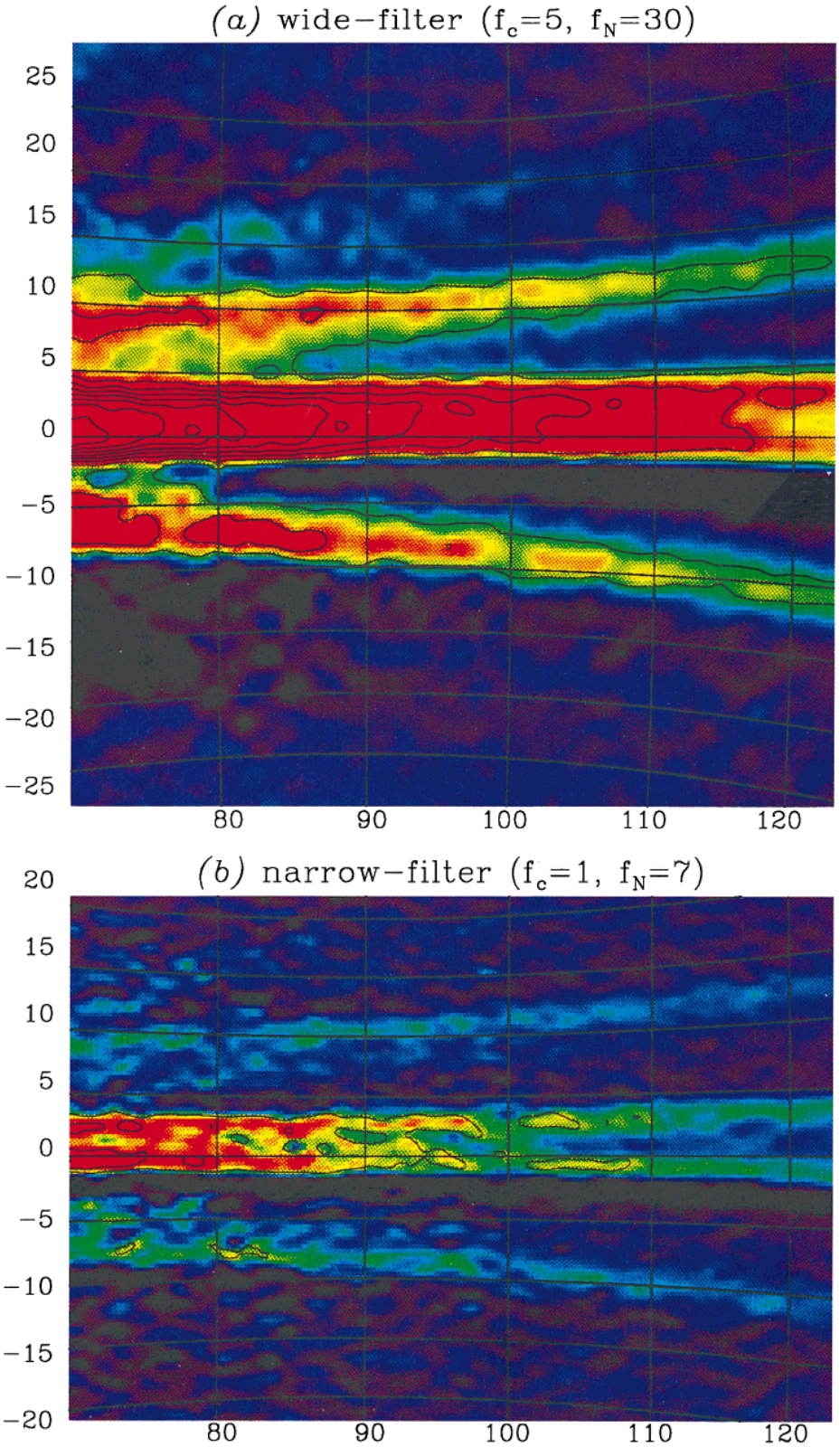

FIG. 2. Fourier-filtered sky brightness at 25 μm, from the DIRBE monthly zodiacal light maps for February 1990. The top panel has been processed to pass emission with vertical angular scales between 3° and 15°, and the botton panel uses a Fourier filter that passes emission with vertical angular scales between 1° and 7°. The projection is part of a face of a quadrilaterized sphere, which is the native pixelization scheme used in analyzing the DIRBE data. Grid lines of differential ecliptic longitude ($\lambda - \lambda_\odot$) and ecliptic latitude (β) are superposed and labeled. The color table is according to the rainbow, with faint levels deep blue and bright levels red. The $\pm 10°$ band pair, associated with the Eos asteroid family, is clearly evident in both panels as two curved regions of enhanced brightness, with the northern component stretching from $(\lambda - \lambda_\odot, \beta) \simeq (70°, 9°)$ to (120°, 13°) and the southern component stretching from (70°, −6°) to (120°, −11°). The separation between the northern and southern components of each dust band increases systematically with distance from the Sun due to parallax (see text). The bright dust band through the middle of both panels, but clearly resolved only in the lower panel, is the $\pm 1.4°$ band pair, associated with a combination of the Koronis and Themis asteroid families. In the upper panel, emission from another band pair is evident at $\pm 17°$ latitude; we associate this dust band with the Maria asteroid family.

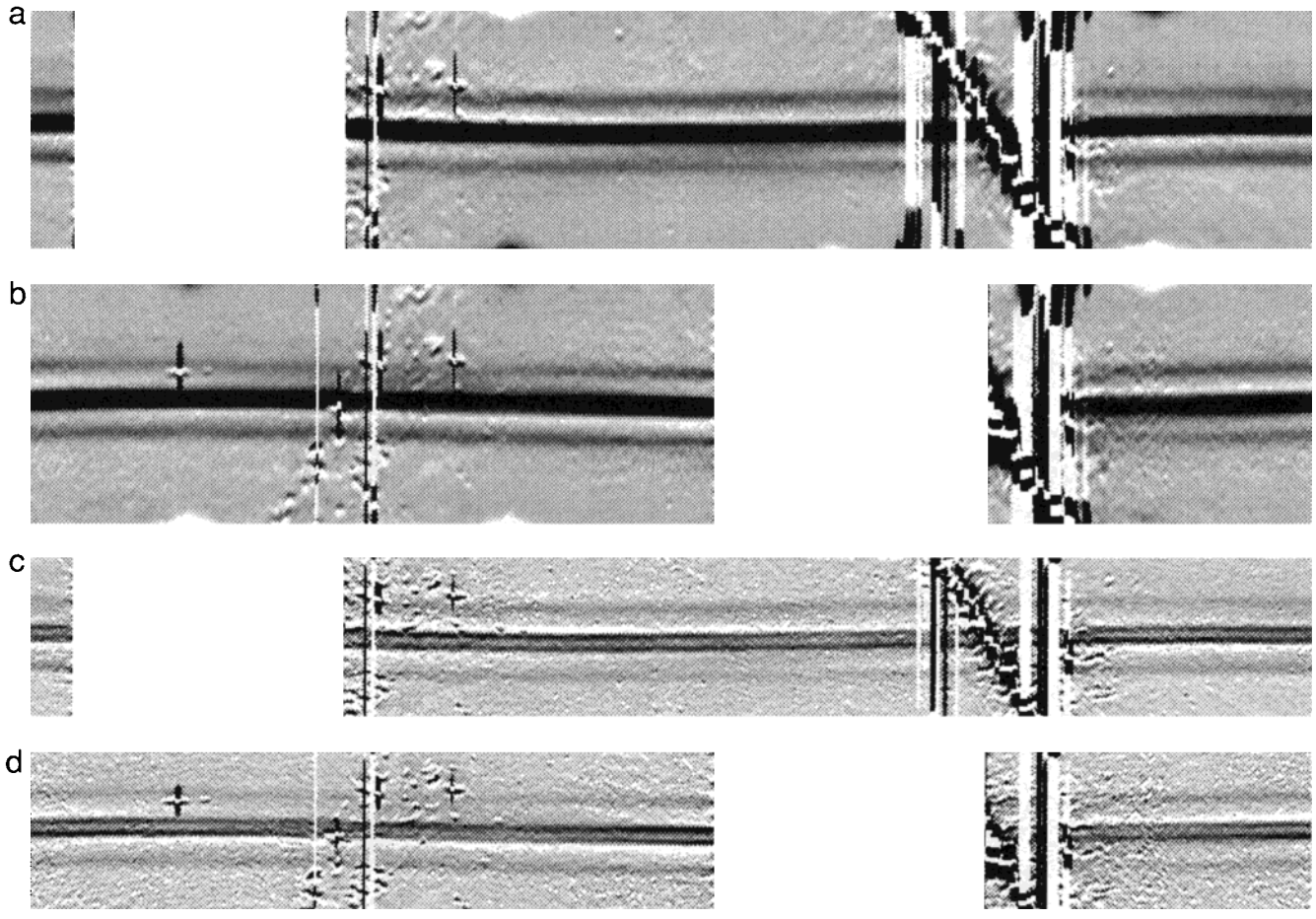

FIG. 3. Sky brightness at 25 μm from DIRBE skymaps using only observations at 90° from the Sun. Panels (a) to (d) from top to bottom. (a) Observations trailing the Earth ($\lambda < \lambda_\odot$), with Fourier filter passing emission on 3° to 15° angular scales. (b) Observations leading the Earth ($\lambda < \lambda_\odot$), with Fourier filter passing emission on 3° to 15° angular scales. (c) Observations trailing the Earth ($\lambda < \lambda_\odot$), with Fourier filter passing emission on 1° to 7° angular scales. (d) Observations leading the Earth ($\lambda < \lambda_\odot$), with Fourier filter passing emission on 1° to 7° angular scales.

bands) and the descending node (at 262 ± 5° for the ±1.4° bands and at 268 ± 4° for the ±10° bands) occurred during the COBE mission, and they are separated by 176 ± 6°, consistent with the 180° separation expected for the intersection of a plane with the Earth's orbit.

TABLE I
Multiple-Gaussian Goodness-of-Fit Dust Bands Included

No. Gaussians	χ^2	−17	−10	−1.4	0[a]	+1.4	+10	+17	Other
3	8.9		√		√		√		
4	4.8		√	√		√			
5	5.7	√	√		√		√	√	
6	2.2	√	√	√		√	√	√	
7	1.4	√	√	√		√	√	√	√
8	1.1	√	√	√		√	√	√	√√

[a] Blend of −1.4° and +1.4° bands.

E. Search for Faint Dust Bands

To reach the ultimate sensitivity limit of the DIRBE observations for detecting faint dust bands similar to those already detected, the data must be coadded in a way that maintains coherence of features with the morphology of dust bands. The monthly maps are already coadded over time as much as is possible before the changing location of the Sun, which is both the approximate geometric center as well as the heating source of the dust, smears the paralactic variation of dust-band latitude with solar elongation. Similarly, the elongation-90 maps can include only a narrow range of solar elongations before systematic variations of the brightness make it impossible to see faint features. Thus it is possible only to view small portions of the DIRBE data without smearing the dust bands.

The dust-band brightness, however, varies relatively mildly with ecliptic longitude, and the variation of the latitudes with longitude is very nearly sinusoidal. There-

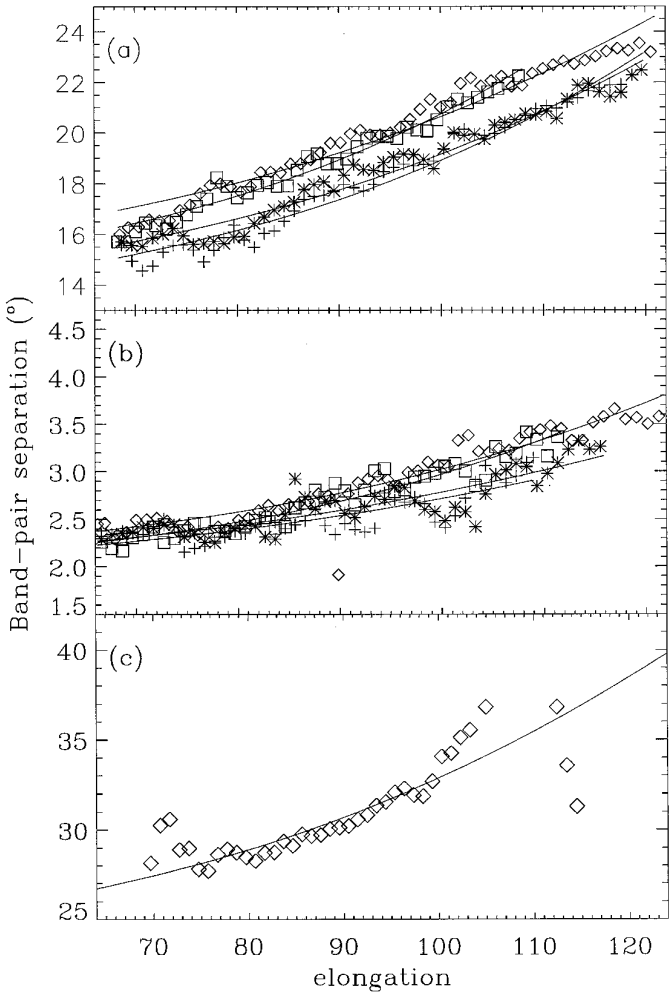

FIG. 4. Separation between northern and southern components of the (a) ±10°, (b) ±1.4°, and (c) ±17° band pairs plotted as a function of the solar elongation. Symbols are coded to indicate the wavelength and the direction (leading or trailing) of the observations, with ◇ and + for 25 μm leading and trailing, and □ and ∗ for 60 μm leading and trailing, respectively. The separations for the ±17° band pair are shown only for 25-μm leading observations; they are much more difficult to measure because of confusion from galactic emission and sidelobes of the ±10° bands.

fore, a first-order ''correction'' can be made that allows profiles at different longitudes to be coadded. We shifted each column in the elongation-90 maps by the centroid of the ±1.4° dust band. We assume that the other dust bands have tilts and nodes not greatly different from those of the ±1.4° bands, which is evidently true for the ±10° bands. Then we averaged the cleanest columns—those without strong galactic emission and away from the beginning and end of the mission—to produce a profile of the surface brightness. The profile derived from the relatively high spatial frequency DIRBE map (Fig. 3, bottom panels) is shown in Fig. 6. Features in this profile are all likely to be ''real'' sky features; fluctuations due to detector noise are negligible. The ±1.4° and ±10° band pairs are clearly evident, as are some other similar features that are nearly symmetrically located with respect to the ecliptic. The ±17° band pair is present but weak in this profile, because the Fourier filter used in this figure decreases the amplitude of wide features. Two other potential band pairs are evident at ±13° and ±6°. The centroid of the ±6° band pair is noticeably nonzero in this profile, indicating that its midplane orientation is significantly different from that of the ±1.4° band pair.

To determine whether they are true band pairs, it must be confirmed that they extend across all ecliptic longitudes. These fainter band pairs are not readily evident in the DIRBE maps, but they are all evident in the IRAS maps produced by Sykes (1988), who identified and labeled them. While the bands are nearly straight and extend over a wide range of longitudes, there are some gaps. The fact that the bands are faint even in the IRAS maps makes it difficult to assess whether the gaps are true breaks in the bands or places where the scan pattern and galactic confusion make the bands undetectable. The evidence is strong enough that we consider the faint bands to be real. Because they are so faint, we will not compare them in detail to three-dimensional models. We will, however, return to them later when assessing the total number of dust bands and their relationship to asteroid families.

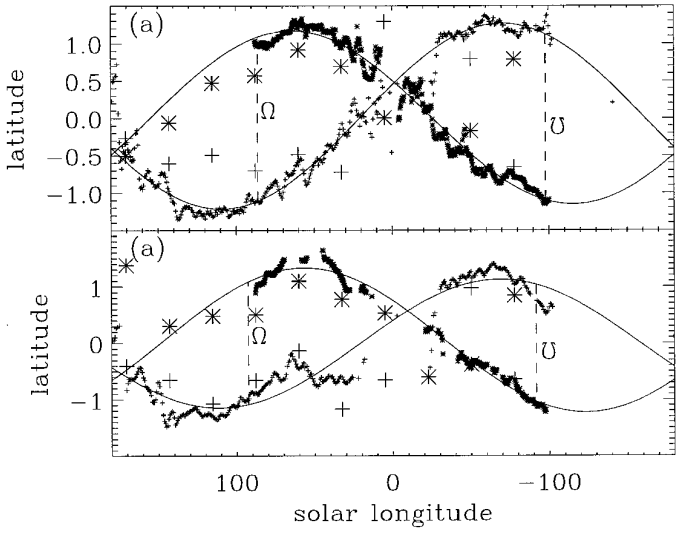

FIG. 5. Centroid of the ±1.4° (a) and ±10° (b) band pairs, plotted as a function of the ecliptic longitude of the Sun. Symbols are coded to indicate the wavelength and the direction (+ for leading or ∗ for trailing) of the observations. Small symbols were derived from the elongation-90 maps, while larger (more sparse) symbols were derived from the monthly skymaps. The ascending and descending nodes, where the centroid is equal and opposite for leading and trailing observations, are indicated by vertical lines.

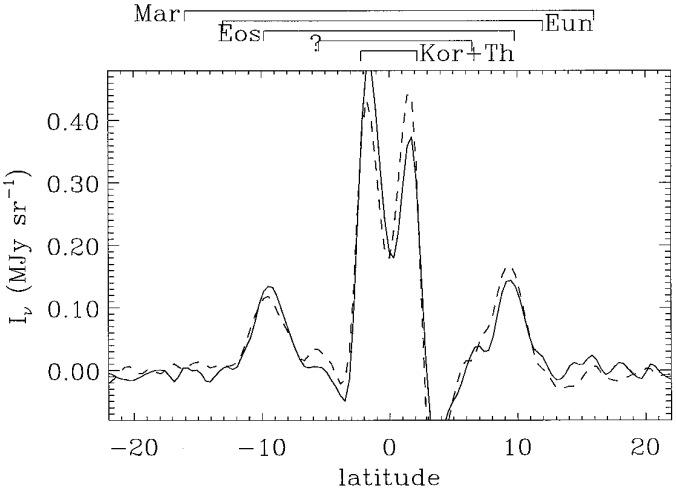

FIG. 6. Surface brightness profile (at 25 μm) obtained from the DIRBE, elongation-90°, Fourier-filtered (1–7° scale) skymap, after rotating to compensate for the tile of the dust-band midplane. Several band pairs are indicated and labeled by the asteroid family with which they are associated: K + T, Koronis + Themis families (blended); Eun, Eunomia/Io family; M, Maria family. The structure labeled "?" remains unidentified.

F. Brightness Variations of the Dust Bands

A qualitatively new effect is evident in the DIRBE elongation-90 maps: the brightness of the dust bands varies as a function of ecliptic longitude. For the 1.4° bands, the northern component is bright when the southern component is faint, and vice versa. We refer to these phenomena as "glints" for the 1.4° bands. A similar effect is visible for the 10° bands, as discussed below. Inspecting Fig. 3, one can see that the southern component of the ±1.4° band pair has glints in the trailing direction at longitudes around 100–200° and in the leading direction at longitudes around 200–300°. The northern component has glints in the trailing direction from the beginning of the mission to 30° longitude and in the leading direction from 70 to 180°. We infer that the glints are caused by an intersection of the emitting region with the Earth's orbit; that is, the Earth passes through the emitting region. If the Earth passes into the northern component of the band pair, its brightness will increase, whether we observe it leading or trailing the Earth's orbit. In the ecliptic longitude maps shown in Fig. 3, the northern and southern glints are roughly 180° apart, and the leading and trailing maps are roughly 180° out of phase. In this picture, the brightness as a function of longitude is directly related to the density of the dust band as a function of distance from its midplane, and we map the density by moving vertically within the dust band.

In the DIRBE maps, the ±1.4° band pair is a blend of the Koronis and Themis dust bands. If the Koronis and Themis dust orbits have significantly different ascending nodes near 1 AU, then we expect the glint pattern to be repeated with two phases. Furthermore, the glint pattern for each individual band pair can have two distinct morphologies. The tilt of the dust-band midplane corresponds to the forced inclination, i_f, due to planetary perturbations (Dermott *et al.* 1985). The half-separation between northern and southern components of a band pair corresponds to the proper inclination, i_p, of the orbits. The scenario we described above, with one glint per year per northern (and southern) component, describes the situation when $i_f \leqslant i_p$. If, on the other hand, $i_f > i_p$, then the Earth will pass completely through each component of the dust band, emerging from the entire cloud twice a year. In this case, there are 2 glints per component per year. Thus in all, we might expect up to 4 glints per component per year (for both the Themis and Koronis families). Further substantial complications of the picture occur because the forced inclination of the particles at 1 AU is different than in the asteroid belt (Dermott *et al.* 1996). Thus, even though the edges of the dust bands in the spatially filtered map have a well-defined sinusoidal variation of latitude (suggesting their origin as a planar sheet of material), the entire dust torus from an asteroid family has a warped surface, with the warp depending on particle size. Because of the confusion of the observed brightness distribution as well as the complexity of the anticipated variations, we do not address this effect in detail in the remainder of this paper.

The ±10° dust-band brightness also varies with ecliptic longitude, and the variation is qualitatively similar to that observed for the ±1.4° dust bands. The brightness of the dust band is correlated with its ecliptic latitude: when the dust band is closer to the ecliptic, it is brighter. For the ±1.4° bands, the brightness varies with longitude by ~50%, and for the ±10° bands, the brightness varies with longitude by about 25%. This effect is simply explained as a reflex of the vertical motion of the Earth within the dust-band torus. The dust density is relatively higher at the northern and southern edges of the torus, and we observe higher surface brightness when we are closest to the edges. The brightness variations would not occur if the material responsible for the dust bands were located in the asteroid belt (Dermott *et al.* 1985, Sykes and Greenberg 1986). Thus the brightness variation is another indication that the ±1.4° and ±10° dust bands must contain particles in Earth-crossing or near-Earth-crossing orbits.

G. Brightness and Spectrum of the Dust Bands

The dust bands are evident in several of the DIRBE wavebands, and the spectral energy distribution of the dust bands is one of the most important observational properties that will allow us to distinguish between different models for their nature. We confirm the detection of the dust-bands at 1.25 μm in the DIRBE data (Spiesman *et al.*

1995), with an albedo for 90° scattering of ~0.08 and an albedo normalized by the Hong (1985) phase function of ~0.15. The dust bands are observable in both thermal emission and scattered sunlight, and they should therefore be observable at visible wavelengths. The fact that they eluded detection until the advent of infrared space astronomy is largely due to their low contrast and large angular size.

Accurate photometry on the dust bands is problematic because they are extended, low-contrast features with a spectrum not dissimilar from that of the zodiacal light. For this work, we measure the spectrum of the dust bands from the Fourier-filtered maps, keeping in mind that the filtering probably removes part of the dust bands themselves, which have power on a wider range of angular scales than passed by our filter; the results obtained in this section can only be compared with similarly processed theoretical predictions. Slices through monthly zodiacal light maps at 12, 25, 60, and 100 μm that were Fourier-filtered to enhance the small-scale dust bands are shown in Fig. 7. The amplitudes of Gaussians fitted to the peaks of the inner dust bands are shown in Table II. Similarly, slices through maps filtered to enhance the larger-scale dust bands are shown in Fig. 8. The inner dust bands are present but blended, so we fitted them with a single Gaussian (just to keep them from interfering with the other bands). The ±10° bands are clearly seen at 12–60 μm and perhaps at 100 μm. The "noise" level is substantially higher in the 100-μm maps; this noise is not only instrumental noise but primarily galactic infrared emission, which is smeared throughout the images by our monthly averaging (despite our attempts to remove the galactic emission by subtracting a template based on the H I column density). The fact that the galactic 100-μm emission can occasionally mimic the dust-band morphology was also found to be a limiting factor in observing them with the IRAS data (Love and Brownlee 1992). We include in Table II photometry for the ±17° bands at 12–60 μm and photometry for the other bands at 1.25 μm derived from maps coadded over 2 months.

The 100-μm and longer-wavelength emission from the dust bands is only marginally detected. The spectrum of the ±10° dust band at 12, 25, and 60 μm is approximated by a blackbody with a temperature of 208 K. Extrapolating this fit to the DIRBE 100-μm waveband one expects 0.2 MJy sr^{-1}, which is smaller than the level of fluctuations due to galactic emission. Similarly, the spectrum of the ±1.4° dust band at 12, 25, and 60 μm is approximated by a blackbody at 250 K. Extrapolating to 100 μm, one expects 0.1 MJy sr^{-1}, which is again comparable to galactic and instrumental "noise," but is consistent with the Gaussian fit results. The spectrum we obtain here for the ±10° dust band is somewhat warmer than that obtained in an earlier analysis of the DIRBE data, in which the +10° dust band was found to have a color temperature of 185 K (Spiesman *et al.* 1995). Part of the difference is due to an improved calibration of the DIRBE data, but most is due to pro-

TABLE II
Brightness of the Dust Bands and Zodiacal Light[a]

Wavelength (μm)	±10°	±1.4°	±17°	Zodiacal light[b]
1.25	0.005 ± 0.001	0.009 ± 0.002	—	0.40
12	0.26 ± 0.05	0.29 ± 0.04	0.08 ± 0.02	36.7
25	0.75 ± 0.05	0.61 ± 0.06	0.2 ± 0.03	69.0
60	0.41 ± 0.05	0.24 ± 0.04	0.13 ± 0.03	21.8
100	0.3 ± 0.2	0.18 ± 0.1	—	7.7

[a] Surface brightness in MJy sr^{-1}.
[b] Zodiacal light model at elongation 90°, latitude 0°.

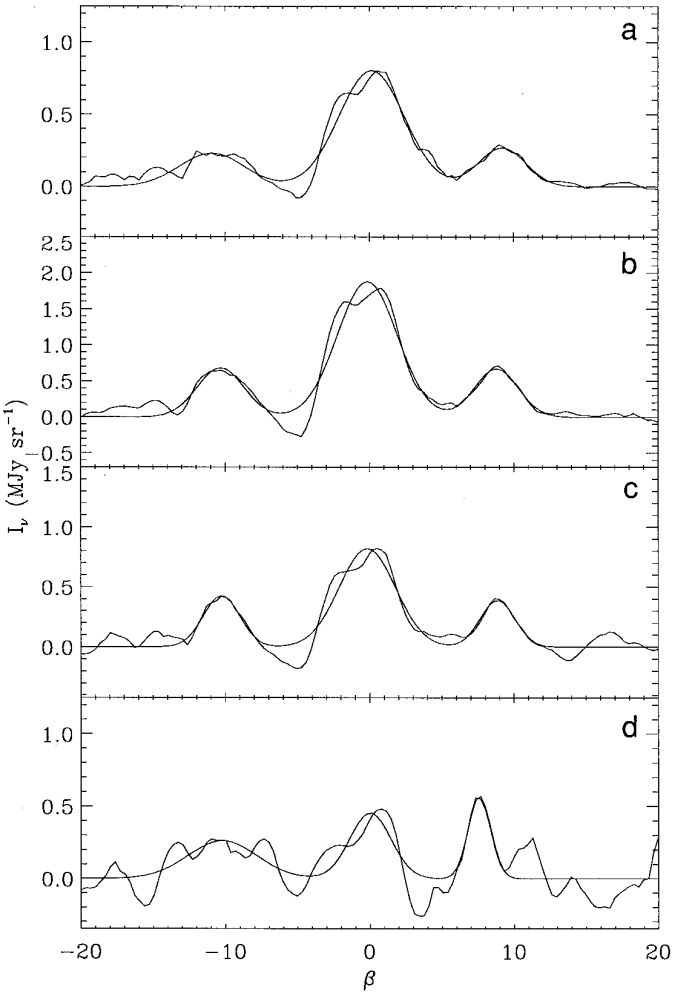

FIG. 7. Latitude profiles at wavelengths of (a) 12 μm, (b) 25 μm, (c) 60 μm, and (d) 100 μm from Fourier-filtered maps that emphasize emission on angular scales between 1° and 7°. A three-Gaussian fit is superposed as a smooth curve approximating the observations. (ε = 88°, leading Earth's orbit).

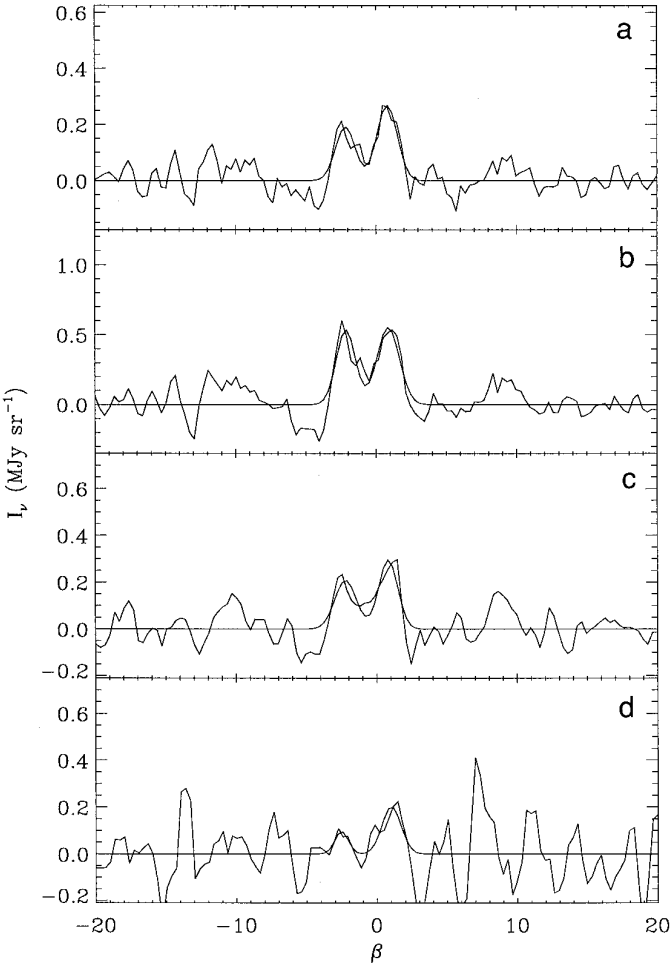

FIG. 8. Latitude profiles at wavelengths of (a) 12 μm, (b) 25 μm, (c) 60 μm, and (d) 100 μm from Fourier-filtered maps that emphasize emission on angular scales between 3° and 15°. A two-Gaussian fit is superposed as a smooth curve approximating the observations. ($\varepsilon = 88°$, leading Earth's orbit).

cessing techniques, underscoring the difficulty of spectrophotometry of the dust bands.

The color temperature of the dust bands is noticeably cooler than that of the zodiacal light itself. Using a three-dimensional model of the interplanetary dust distribution, optimized to match the time variation of the brightness observed by DIRBE (Reach *et al.* 1996b), the brightness of the zodiacal light on Day 100 perpendicular to the Earth's orbit ($\varepsilon = 90°$) and in the ecliptic ($\beta = 0°$) is listed in Table II. The color temperature between 12 and 25 μm is 260 K, while between 25 and 60 μm, it is 320 K. Recent observations of the spectrum between 5 and 16 μm by the midinfrared camera on the Infrared Space Observatory find a temperature around 262 K for a line of sight at 100° elongation; the temperature and the lack of spectral features support a "dirty silicate" composition and particle sizes ~10–200 μm producing the zodiacal emission (Reach *et al.* 1996a). Evidently the 60-μm emission is depressed with respect to the nearly blackbody spectrum from 5- to 25-μm brightnesses because the grains do not emit efficiently at wavelengths larger than their size; the 60-μm emissivity is about 0.7 for the zodiacal light (Reach *et al.* 1996a). It is possible to model the dust bands using a single temperature for the 12-, 25-, and 60-μm bands, yielding a color temperature of 208 K. Thus not only is the color temperature of the dust bands cooler than that of the zodiacal light, but also the spectral shape is different. This could indicate that the dust-band particles are larger than the zodiacal light particles on average (because larger particles emit efficiently at long wavelengths). On the other hand, if the emitting region is spread over a wide range of heliocentric distances, the spectrum is coupled to the radial distribution, so it is not straightforward to interpret the spectrum of the line-of-sight integrated radiation without a three-dimensional model.

H. High-Resolution IRAS Maps

To see the structure of the dust bands on scales smaller than the 42′ beam of DIRBE, we created an image of the ecliptic plane from the IRAS Infrared Sky Survey Atlas (ISSA, Wheelock *et al.* 1994). A model for the zodiacal light has been removed from the ISSA (Good 1994), but this model included only a smooth functional form that does not remove the peaks of the dust bands. It may remove the larger-scale portion of the dust-band emission, but we will consider only spatially filtered observations that are not much affected by the zodiacal light subtraction. The image is a mosaic of 17 ISSA plates, covering a $40° \times 20°$ area centered on ecliptic longitude $\lambda = 355°$ and latitude $\beta = 0°$, using the HCON 2 data only. This region is free of significant galactic dust emission, as evident by the lack of significant structured 100-μm emission. The individual plates were reprojected onto a cylindrical projection with 800×400 square pixels. Profiles of the surface brightness as a function of ecliptic latitude were constructed by coadding in four 200-column ranges of ecliptic longitude, and the profiles were spatially filtered by removing a boxcar average. One of the profiles is shown in Fig. 9. The profiles clearly show four individual peaks. The location of each peak changes nearly linearly with ecliptic longitude, as expected due to the tilt of the midplane with respect to the ecliptic.

III. MODELS FOR THE DISTRIBUTION OF ASTEROID COLLISIONAL DEBRIS

A. Ring-Pair Model

First we describe a simple "model" for the dust bands—with no physical justification—that can be used to calculate

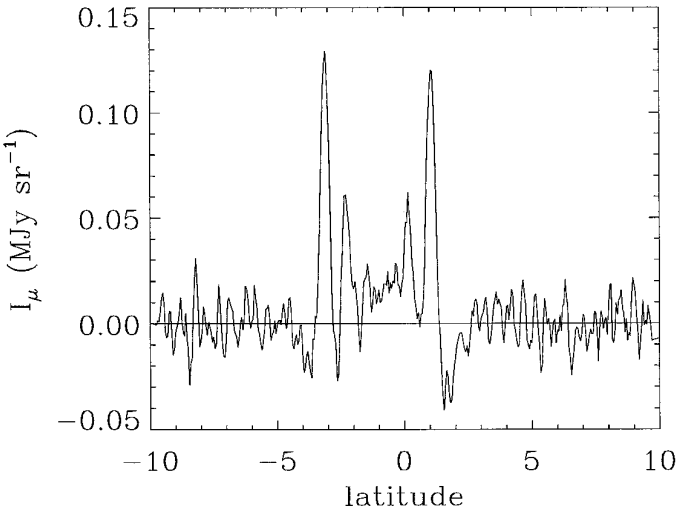

FIG. 9. Spatially filtered 25-μm surface brightness from a mosaic of ISSA plates. The high resolution of the IRAS observations allows the $\pm 1.4°$ dust band to be cleanly resolved into two separate band pairs, which are seen here as four peaks in the surface brightness as a function of ecliptic latitude.

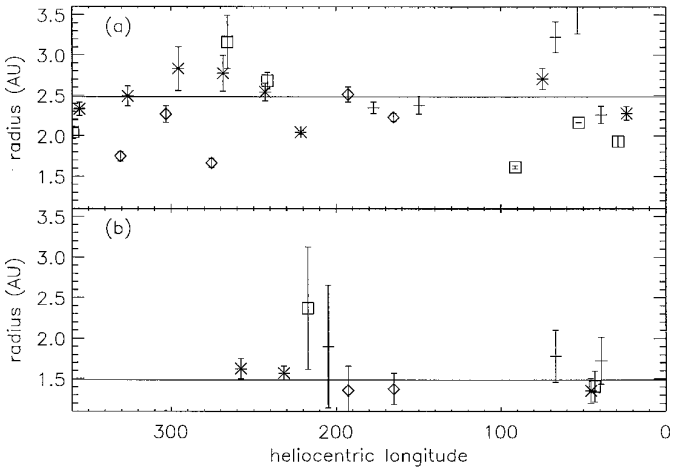

FIG. 10. Parallactic radius of the $\pm 10°$ band pair (a) and the $\pm 1.4°$ band pair (b), plotted as a function of the heliocentric longitude of observations. Symbols are coded as in previous figures to indicate the wavelength and the direction (leading or trailing) of the observations.

their locations to first order. We suppose the apparent "band pairs" on the sky correspond to "ring pairs" in three dimensions. The rings are presumed parallel to each other, but tilted with respect to the ecliptic. The ring-pair system is described by the vertical separation, the ring radius, and the ring thickness. Equations for the separation of the band-pair latitudes as a function of solar elongation and observation date are given in an earlier paper (Reach 1992). One example of a fit to the parallactic observations is shown in Fig. 4. Few of the months were as easy to interpret as that shown in Fig. 4, because the Milky Way crosses through the viewing swath and makes it impossible to measure the latitude of either the northern or southern component of a band pair during part of the mission. In Fig. 10, the parallactic radius is displayed as a function of the heliocentric longitude for each observation for which it was possible to measure the radius. (The heliocentric longitudes refer to the location where the line of sight crosses a ring with the parallactic radius.) There is evidently no trend of radius with longitude. We can use these observations to place a weak limit on the forced eccentricity of the particles: $e_f < 0.15$ for the $\pm 10°$ band pair, and $e_f < 0.2$ for the $\pm 1.4°$ band pair. These limits are much larger than the eccentricities deduced from numerical and analytical studies of particle orbits under the influence of planetary perturbations and Poynting–Robertson drag (Dermott *et al.* 1996). A summary of the properties of the ring-pair model is given in Table III. The parallactic radii and tilts are similar to those obtained from a similar analysis of the IRAS data (Reach 1992), but the ascending node is somewhat different.

b. Torus Model

We now consider a more realistic model for the dust bands that has been proposed on physical grounds. The dust bands are presumed to be formed as a result of the collisional disruption of an asteroid (Sykes and Greenberg 1986). After the disruption, the fragments disperse due to the kinetic energy imparted to them. First, they fill the orbit of the progenitor; then they are spread by differential precession by Jupiter to create the torus. The time scale for torus creation is of order 10^6 years. The distribution of particles in the torus was shown graphically by Dermott *et al.* (1985), and equations for the number density were derived by Sykes (1990). For each asteroid family with known mean orbital elements, a dust-band model can be calculated from these equations and compared with the observations; however, there are two complications that make such a calculation uninteresting. First, the dust band could be due to (or dominated by) debris from disruption of an individual family member with orbital elements significantly different from the family mean. Further, the orbital elements of the dust particles will have substantial dispersion, due to the origin from various family members, kinetic energy imparted by the catastrophic disruption that formed them, and the subsequent mutual collisions and

TABLE III
Ring-Pair Model Parameters

Band pair	R_p (AU)	z (AU)	i	Ω
$\pm 10°$	2.4 ± 0.3	0.39 ± 0.06	0.82 ± 0.12	80 ± 9
$\pm 1.4°$	1.7 ± 0.2	0.040 ± 0.007	0.76 ± 0.12	88 ± 9

gravitational perturbations. Sykes (1990) demonstrated the effect of dispersion in the elements by convolving the dust distribution with Gaussian distributions in (a, e, i) with widths (δa, δe, δi). The spread of orbital elements changes the location and shape of the dust bands. The convolutions are computationally time consuming, but an ad hoc equation that approximately reproduces the convolved distribution is

$$n(r,\zeta) = e^{-\left(\frac{r-R_0}{\delta_r}\right)^4}\left(\frac{R_0}{r}\right)^{p_r}\left[1+\frac{1}{v_r}\left(\frac{|r-R_0|}{\delta_r}\right)^{p_{2r}}\right] e^{-\left(\frac{\zeta}{\delta_\zeta}\right)^6}\left[1+\frac{1}{v_i}\left(\frac{\zeta}{\delta_\zeta}\right)^{p_i}\right], \quad (1)$$

where $\zeta \equiv z/r$. The basic parameters for a band are (R_0, δ_r, δ_ζ). The forced eccentricity of the band particles can be taken into account with the parameters (e_f, ω_f) by shifting the center of the distribution from the Sun to a point ae_f away, toward the direction opposite ω_f (Dermott *et al.* 1985). The shape parameters that can be used to tune Eq. (1) are p_r (adjusts perihelion/aphelion ratio), v_r and p_{2r} (adjust sharpness of perihelion/aphelion enhancement), v_i (adjusts central density), and p_i (adjusts sharpness of latitude peaks). The model band shown in Fig. 4 of Sykes (1990) is reasonably reproduced with the nominal parameters $p_r = 1$, $v_r = 0.6$, $p_{2r} = 2$, $v_i = 0.2$, and $p_i = 4$. The radial and vertical profiles of this model are shown in Fig. 11. The vertical and radial edge enhancements, due to the fact that particles spend the most time at the extrema of their orbits, are evident in the model torus as four peaks. The perihelion and aphelion peaks essentially overlap on the sky, so we see a band as a pair of enhancements where the line of sight crosses $\pm\delta_\zeta$.

C. Migrating Band Model

If an asteroid collision is sufficiently old, then it loses particles due to the Poynting–Robertson effect. A particle with radius s (>0.1 μm) in a circular orbit with semimajor axis r is predicted to spiral into the Sun in (Burns *et al.* 1979)

$$\tau_{PR} = 700 Q^{-1} \rho s r^2 \text{ years}. \quad (2)$$

Here Q is the coupling efficiency between the solar radiation pressure and the particle; for particles with $s > 1$ μm, $Q \simeq 1$. Based on the size distribution of particles collected in Earth orbit, the zodiacal emission is produced by particles with radii of order 10–100 μm (Reach 1988). Thus, if they start at $r = 3$ AU, particles of the size that produce the zodiacal emission would spiral into the Sun in 10^5 to 10^6 years. This is in fact faster than the time it takes to form a torus by differential jovian precession (Sykes and Greenberg 1986). Therefore, particles produced by collisional comminution in the present dust torus are expected to be spiraling in toward the Sun. The continuity equation for the Poynting–Robertson effect leads to a density of such particles proportional to $1/r$. Therefore, the toroidal distribution originally considered by Dermott *et al.* (1985) and Sykes (1990) is unlikely to apply to the dust. The torus model is effectively identical to the ring-pair model, if only the spatially filtered brightness is considered. Observations of the parallax and color temperature of the dust bands by IRAS (Reach 1992) and by DIRBE (Tables II and III; also Spiesman *et al.* 1995) have already revealed that the dust-band emission is apparently not coming from the asteroid belt. The parallactic radii deduced above are in disagreement with the torus model for the major asteroid families, for which $R_p \simeq q \simeq 2.7$–2.8 AU.

We consider now an alternative model that incorporates the toroidal distribution of material expected from the orbital elements of the debris, as well as the expected transport of particles into the inner Solar System by Poynting–Robertson drag. The bands are presumed to have a vertical structure similar to Eq. (1), but a radial structure that is $1/r$ out to the asteroid belt. This model was compared with the IRAS observations and found able to predict the parallax, color temperature, and width of the observed dust bands (Reach 1992). A migrating band model may be obtained by setting $\delta_r \gg 1$, $p_r = 1$, $e_f = 0$, and $v_r > 1$, so that Eq. (1) becomes

$$n(r,\zeta) = \frac{R_0}{r} e^{-\left(\frac{\zeta}{\delta_\zeta}\right)^6}\left[1+\frac{1}{v_i}\left(\frac{\zeta}{\delta_\zeta}\right)^{p_i}\right]. \quad (3)$$

The tilt of the bands (i_f, Ω_f) can be included in a coordinate transformation, so that ζ is relative to the midplane of the dust. The forced eccentricity is neglected here because the particles do not have a common heliocentric distance. Numerical simulations of orbits starting in the asteroid belt and evolving under Poynting–Robertson drag and planetary perturbations show that the forced eccentricity varies from $e_f = 0.04$ at $a = 2.5$ AU to $e_f \simeq .014$ at $a \simeq 1$ AU (Dermott *et al.* 1996); these small eccentricities can be safely neglected in our three-dimensional models. Slices through a migrating model for the Eos asteroid family are shown in Fig. 12, for comparison with the torus model density map in Fig. 11. The vertical distribution has the same edge-brightening effect as for the torus model, which leads to the band-pair morphology on the sky.

Unlike the torus model, there is a noticeable difference between the morphologies of the migrating model maps at different wavelengths. The peaks, which we view as the "bands" on the sky, are broader at 12 μm than at 60 μm. The brightness of dust at a given distance from the Sun is proportional to the volume density weighted by the Planck function at the dust temperature appropriate to that dis-

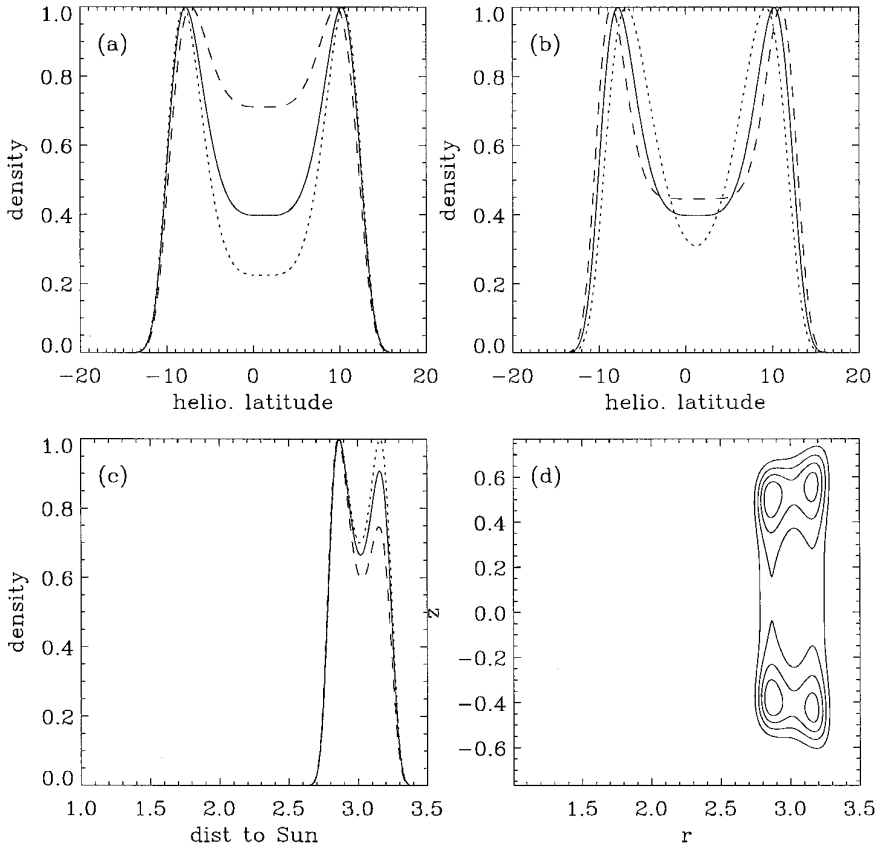

FIG. 11. Torus model. (a) Vertical profile of the model torus with the nominal parameters and two other values of v_i, showing the effect of v_i on the central density. (b) Vertical profile for nominal profiles and two other values of p_i, showing the effect of p_i on the sharpness of the high- and low-latitude peaks. (c) Radial profile for the nominal parameters and two other values of p_r, showing the effect of p_r on the density of the inner edge of the torus relative to the outer edge. (d) Map of a cut through the model torus in the r–z plane.

tance. Dust near 1 AU (3 AU) has a temperature of 280 K (160 K), and its spectrum peaks around 18 μm (32 μm). The DIRBE 12-μm waveband is dominated by dust in the Wien portion of the spectrum, for which the brightness is a very steep function of the temperature. Thus at 12 μm, the emission is dominated by the part of the line of sight closest to the Sun. This portion of the line of sight is relatively closer to the Earth (for lines of sight with solar elongation greater than 90°), so the 12-μm emission will appear to occupy a larger angular extent out on the sky.

Because of the different mean heliocentric distances of the emitting regions, the spectra predicted by the migrating and torus models are significantly different. For the torus model, the spectrum is largely determined by the temperature of particles at perihelion. The families with the brightest dust bands have q = 2.7–2.8 AU, so the infrared dust-band emission is expected to have a color temperature around 170 K, if the optical properties of the asteroidal debris are similar to those of interplanetary dust particles near the Earth. For the migrating model, the emission derives from all along the line of sight, with weighting toward nearby positions. As a result, the 12-μm emission is brighter than the 60-μm emission for the migrating model, while the opposite is true for the torus model. The observed spectrum of the dust bands (Figs. 7 and 8) is indeed warmer than the 170 K predicted by the torus model. Combined with the fact that the parallactic radius of the emitting region is smaller than that of the asteroid belt, the relatively warm observed spectrum supports the migrating model.

The fact that the migrating model predicts dust crossing the Earth's orbit has two important implications. First, we note that the migrating model predicts a nonnegligible brightness toward the ecliptic poles. Thus those who hope to model the zodiacal light to search for the cosmic infrared background radiation must consider a contribution from the dust bands even in the faintest parts of the sky (Hauser 1996, Reach *et al.* 1996b). Second, we note that if a dust band is sufficiently inclined with respect to the ecliptic, then the migrating model predicts that the Earth will actually pass through the dust bands in the course of year. If our interpretation of the brightness variations of the ±1.4°

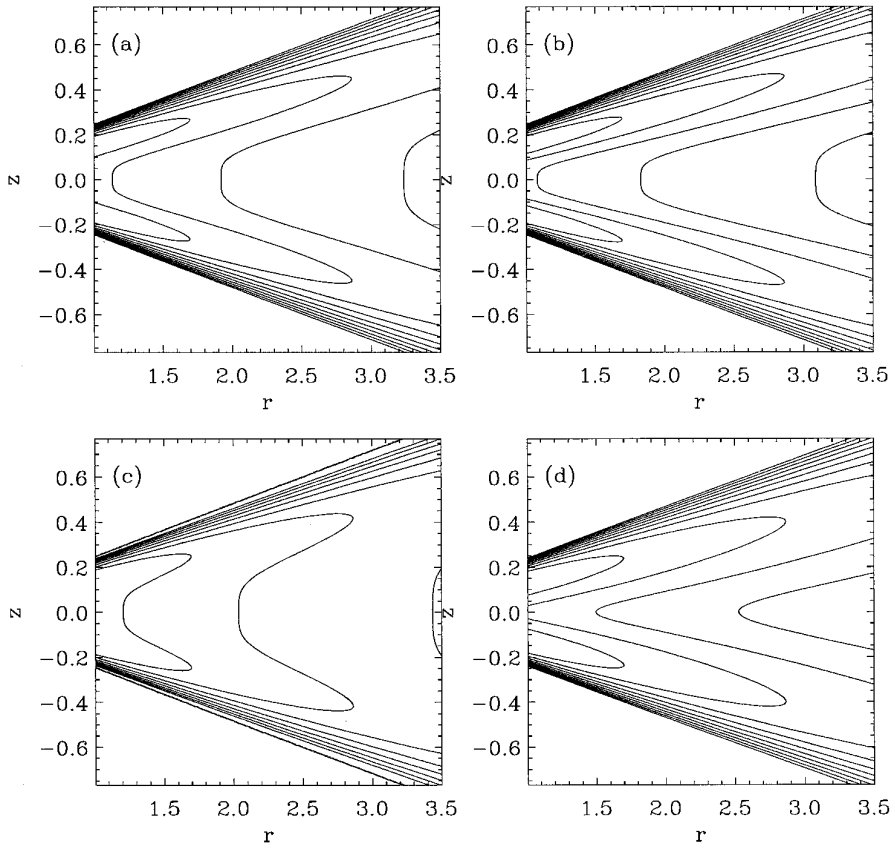

FIG. 12. Slices through a sample migrating band model in the r–z plane. Each panel shows contours of the density normalized to the peak, with contours spaced logarithmically by factors of 1.58. (a) Nominal parameters, (b) $v_i = 0.1$, (c) $v_i = 0.5$, (d) $p_r = 0.75$.

and $\pm 10°$ dust bands is correct, then the detection of this effect conclusively rules out the ring-pair or torus models.

D. Jones and Rowan-Robinson Model

A substantially different model for the interplanetary dust cloud shape was proposed by Jones and Rowan-Robinson (1993; hereafter, JRR). It is asserted by JRR that they propose a physically justifiable model of the dust cloud, but in fact they have made the following ansatz: "An assumption of the model is that the zodiacal cloud is formed by the perturbations of the dust in asteroidal bands as it passes close to the orbit of Mars." This assumption is both theoretically unjustified and in conflict with observations by spaceprobes that have flown past Mars. In the JRR model, the zodiacal cloud consists of two parts: a smooth cloud extending out to Mars' orbit, then a banded cloud between Mars' orbit and the asteroid belt. Mars is a very small planet, and its gravity does not exert much influence on dust dynamics. Jupiter is 3000 times more massive and, besides the Sun, dominates gravitational forces for particles more than 0.1 AU from Mars. Terrestrial planets do have some influence on asteroidal dust, through resonances. Earth has been shown to temporarily trap particles in mean-motion resonances, leading to a circumsolar dust ring with radius just outside the Earth's orbit (Jackson and Zook 1989, Dermott *et al.* 1994a, Reach *et al.* 1995). A similar ring due to resonant trapping by Venus may be evident in the Helios spaceprobe observations (Reach, Leinert, and Jayaraman, in preparation). Mars may produce a similar (but probably much smaller) ring due to orbital resonances. But numerical simulations show that the banded distribution of asteroidal dust persists as particles spiral inward past Mars (Dermott *et al.* 1994b).

There is direct observational evidence that Mars does not significantly affect the structure of the zodiacal cloud. the zodiacal light has been observed by spacecraft that went past Mars' orbit, notably Pioneer 10 (Hanner and einberg 1974). Particle detectors have also flown through the cloud, notably aboard Galileo (Grün *et al.* 1995a) and Ulysses (Grün *et al.* 1995b). The volume density of interplanetary dust near the ecliptic apparently does not have an abrupt decrease beyond 1.52 AU, in contradiction with the JRR model. In fact, the Pioneer 10 zodiacal light obser-

TABLE IV
Largest Asteroid Families

Family	i'	σ_i	a′	σ_a	e'	N^a
Themis	1.359	0.166	3.142	0.043	0.15	267
Koronis	2.105	0.042	2.865	0.028	0.049	147
Nysa	2.695	0.477	2.398	0.055	0.17	107
Flora	4.457	1.508	2.240	0.015	0.14	338
Eos	10.112	0.270	3.015	0.007	0.074	220
Eunomia	13.113	0.311	2.626	0.038	0.15	100
Maria	14.986	0.208	2.555	0.016	0.094	38

[a] Number of members that are numbered asteroids (Zappalá *et al.* 1994).

vations, which are sensitive to the same particles we are observing with DIRBE, suggest that the density decreases smoothly as $r^{-1.5}$ from the Earth's orbit to at least 3 AU. Thus, the observations show no effect in the dust distribution due to Mars. For these reasons, we do not consider the JRR model in detail here.

IV. COMPARISON OF THREE-DIMENSIONAL MODELS TO THE OBSERVATIONS

A. Largest Asteroid Families

To compare the dust-band observations to models of their origin in asteroid families, we must first identify the set of plausible parent families. Asteroid family identification is based on concentrations in the phase space of the proper orbital elements (a', e', i'), which must be calculated from the osculating orbital elements using a theory of planetary perturbations. The number and population of asteroid families are contentious owing to the variety of numerical methods to calculate the proper elements, observations sufficiently accurate to determine orbits, and, most importantly, methods to decide which concentrations in (a', e', i') constitute families (cf. Carusi and Valsecchi 1982). Zappalá *et al.* (1990, 1994) identified families using numbered and multiopposition asteroids, the perturbation theory of Milani and Knežević (1990), and an automated, objective, hierarchical clustering technique. The seven largest asteroid families from Zappalá *et al.* (1994), named after their least-numbered member and in order of increasing proper inclination, are listed in Table IV. Williams (1992) identified families visually from stereoscopic projections of the three-dimensional phase space distributions, and then evaluated the likelihood of each visually identified family using Poisson statistics for comparison with a random background. Williams' procedure resulted in a much larger number of families, and in particular it breaks some of the Zappalá *et al.* families into subfamilies. If we consider the number of "numbered" (i.e., accepted and with well-known orbit) asteroids in each family, and recognize Williams' families 180–189 as subunits of Zappalá's Flora family, then the same seven largest families are obtained. For comparison, Sykes (1990) considered essentially the same families, with the concentration at proper inclinations around 13° named for Io instead of Eunomia. Thus despite disagreement about the total number of families and the substructure of families, the identification of the largest asteroid families seems robust. Using the asteroid proper orbital elements of Milani and Knežević (1990), we measured the mean and (Gaussian) dispersion of a' and i' (after restricting to the appropriate ranges of eccentricity) for each family; results are listed in Table IV.

B. Nominal Family Models

The dust distribution in an asteroid family can be calculated directly from the distribution of orbital elements, with an arbitrary normalization to be established by comparison with the observations. The parameters in Eqs. (1) and (3) are directly related to the orbital element distributions. Of particular importance is the vertical distribution, which is governed by the mean inclination, i, and its dispersion, δi. By comparing the dust distributions for a range of i and $\delta i/i$ to our models for a range of δ_ζ and v_i, we found the following relations:

$$\begin{aligned} v_i &= 1.05(\delta i/i)^{0.45} - 0.11, \\ \delta_\zeta &= [1 - 1.16(\delta i/i)^{1.13}]/[0.94 - 0.22 v_i]. \end{aligned} \tag{4}$$

We refer to the dust-band model based on the orbital element distributions of the asteroid families as the "nominal family models." Mean orbital elements for the families were measured from the asteroid distribution, as described above, then converted into our model parameters using Eq. (4).

The models were directly compared to latitude-profiles of both the DIRBE and IRAS data. The same spatial filtering was applied to the models as to the data. For the Themis and Koronis families, we used the IRAS data to normalize the models, thus determining the dust density. A slice through the IRAS data is shown in Fig. 13 together with the corresponding nominal torus and migrating models; profiles in this figure were high-pass filtered using a running boxcar with a width of 1°. Similarly, a slice through the DIRBE data is shown in Fig. 13b together with its corresponding nominal torus and migrating models; profiles in this figure were Fourier filtered as described above. It is evident that the models have the correct general morphology and are "the right idea," but the latitude of the dust bands is always inside (i.e., at lower absolute latitude) the models.

C. Optimized Family Models

The nominal family models have the correct general shape, and need only small adjustments to match the obser-

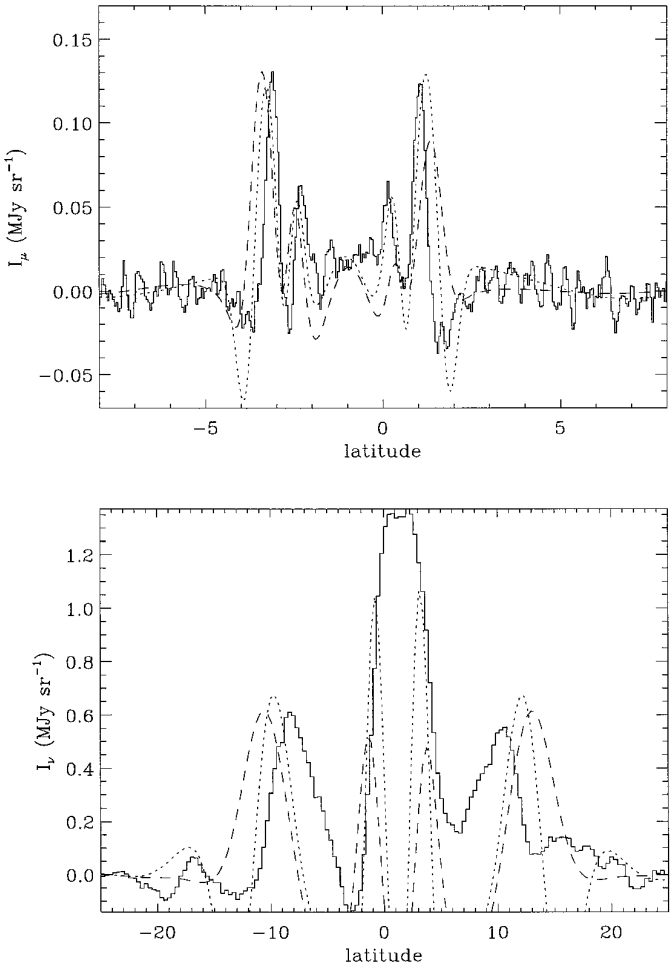

FIG. 13. Nominal family models. (Top) High-pass filtered brightness observed by IRAS (+signs) as a function of ecliptic latitude, together with corresponding torus (dotted line) and migrating (dashed line) models. (Bottom) Fourier-filtered brightness observed by DIRBE (+signs) as a function of ecliptic latitude, together with corresponding torus (dotted line) and migrating (dashed line) models. In all cases, the observed bands are closer together than the models predict.

vations in detail. There are two ways to move the latitudes of the models downward, approaching those of the observed dust band. The obvious way is to adjust the mean inclination of the dust band downward; this translates directly into a vertical shift in the latitudes. The second way is to boost the dispersion in orbital inclinations. This is somewhat more indirect, and it has the side effect of increasing the widths of the northern and southern components of the dust bands at the same time as decreasing their separations.

For the Themis and Koronis families, the models already have the correct angular widths but predict latitudes somewhat too high. We found that shifting the mean inclinations downward was sufficient to bring the models into close agreement. The complete set of parameters for the optimized models is shown in Table V, and the optimized models are plotted together with the IRAS data in Fig. 14.

In addition to the locations of the dust bands, the brightness variations are also predicted by the models. The torus model predicts dust bands with a constant brightness as a function of ecliptic longitude. The migrating model, on the other hand, predicts a strong variation due to the crossings of the Earth through the emitting region. The observed "glints" apparently rule out the torus model, but neither do the glints agree in detail with the migrating model. The migrating model for the Koronis family that matches the observed latitudes of its dust bands is shown in Fig. 15, where we have exactly matched the observing conditions of the elongation-90 skymaps shown in Fig. 3. The observed glints are milder—about 50%—than the factor of 3 variation of brightness predicted by this model. Two effects are likely to contribute to the disagreement. First, we assumed that the dust orbits evolve only due to Poynting–Robertson drag and that their proper and forced inclinations remain unchanged as they spiral into the Sun. This assumption is unlikely to be valid, because planetary perturbations in the inner Solar System are dominated by the terrestrial planets, while those in the asteroid belt are dominated by Jupiter. Thus the midsurface of the dust bands is likely to be significantly warped and the radial distribution significantly perturbed from the assumed $1/r$ distribution. A second effect that could make the longitude variations less severe than the model shown in Fig. 15 is an increase in the dispersion in proper inclinations in the inner Solar System, which might be expected due to the larger collision rate with cometary dust and meteoroids.

For the Eos and Maria families, a shift in proper inclination, in the same direction as (but larger than) that required for the Koronis and Themis families, brings the models into agreement with observed dust-band latitudes. It is also possible bring the models into agreement with the data by boosting the dispersion of orbital inclinations. This effect was used by Sykes (1990) to bring the predicted latitude of the Eos family into agreement with the location of the $\pm 10°$ band on the IRAS SykFlux plates. We found that increasing the Eos dispersion by a factor of 2.5 (torus model) to 3.5 (migrating model) has approximately the same effect as changing the mean inclination, and brings the model latitudes into agreement with the DIRBE observations at elongation 90°. The Maria dispersion needs to be increased by a factor of ~5–10 to match the observed latitude. This seems like a large increase, but in fact the nominal dispersion of the Maria family asteroids is very small. The dispersion of the dust band, $\delta i \sim 2°$, is similar for both Eos and Maria. The dispersion of dust orbits is apparently not directly related to that of the asteroid family.

In addition to testing the vertical shapes of the models

TABLE V
Parameters of Dust-Band Models

Parameter	Themis	Koronis	Nysa	Flora	Eos	Eunomia	Maria
			a. Torus model[a]				
i	1.209	1.955	2.695	4.457	9.112	12.113	14.486
Δi	−0.150	−0.150	0.000	0.000	−1	−1	−0.5
σ_i	0.166	0.042	0.477	1.508	0.270	0.311	0.208
n_0[b]	1.8	5.0	<2	<1	5.0	1.4:	0.9:
R_0 (AU)	3.142	2.865	2.398	2.240	3.015	2.626	2.555
δ_r (AU)	0.236	0.070	0.204	0.157	0.112	0.197	0.120
p_r	1.0	1.0	1.0	1.0	1.0	1.000	1.0
v_r	0.366	0.248	0.663	0.161	0.050	0.390	0.149
p_{2r}	4	4	4	4	4	4	4
δ_ζ	1.219	1.978	2.624	3.570	9.186	12.388	14.910
v_i	0.318	0.075	3.370	0.533	0.104	0.090	0.050
p_i	4	4	4	4	4	4	4
			b. Migrating model[c]				
i	1.209	1.855	2.695	4.457	8.612	11.613	13.986
Δi	−0.150	−0.250	0.000	0.000	−1.500	−1.500	−1.000
σ_i	0.166	0.042	0.477	1.508	0.270	0.311	0.208
n_0[b]	0.25	0.43	<0.4	<0.8	1.0	0.26	0.22
p_r	1.0	1.0	1.0	1.0	1.0	1.0	1.0
δ_ζ	1.219	1.978	2.624	3.570	9.184	12.388	14.905
v_i	0.318	0.079	0.370	0.533	0.109	0.094	0.050
p_i	4	4	4	4	4	4	4
R_0 (AU)	3	3	3	3	3	3	3

[a] Parameters from Eq. (1).
[b] Volumetric cross section ($n\sigma$) at R_0, units 10^{-9} AU^{-1}.
[c] Parameters from Eq. (3).

using the latitude profiles, we have also tested the radial shapes of the models by using the parallactic change of band-pair separation with solar elongation (Fig. 4). We evaluated latitude profiles for a range of solar elongations, and compared these to the DIRBE observations, interpolated to the same grid. The optimal values of the mean semimajor axis for the torus model [R_0 in Eq. (1)] and the radial power-law index for the migrating model [p_r in Eq. (3)] were determined by minimizing the mean square errors. For the Eos family, the best fits were obtained with $p_r = 1.0 \pm 0.3$ (migrating model) and $R_0 = 3.2 \pm 0.3$ AU (torus model). There is a qualitative difference between the parallactic predictions of the torus and migrating models, in that the torus model predicts the separations to increase nearly linearly with solar elongation, while the migrating model predicts a negative curvature. Because some negative curvature is in fact observed, the torus model never achieves a good fit, for any value of R_0.

D. Dust Bands Associated with Other Asteroid Families

The association of bright dust bands with the Themis, Koronis, and Eos families is convincing. The ±17° band pair in the DIRBE data was also found in the IRAS data (Sykes 1988), and its association with the Maria family also seems convincing. Of the largest asteroid families, Nysa, Flora, and Eunomia/Io remain to be discussed. It is important to consider this issue in detail, because we hope to determine whether dust bands are a general phenomenon that should be expected for asteroid families. Nominal models were calculated for each family and compared to the IRAS and DIRBE observations described above. A lack of unexplained low-latitude dust bands in the IRAS data places rather strong limits on the amount of dust associated with the Nysa or Flora family. In Fig. 9, there is no evidence for band pairs in addition to those already discussed.

There remain, however, dust bands in the IRAS and DIRBE data with morphology similar to those already discussed but no parent. The map produced by Sykes (1988) from the IRAS data is the most sensitive search for dust bands and trails, owing to the near-optimal utilization of the data. There are seven band pairs in the IRAS data (see Sykes 1988, Table 1). The α, β, and γ bands correspond to the Themis, Koronis, and Eos families, respectively. The M/N bands correspond to the Maria family as discussed above. The remaining three band pairs are E/F (at ±5°), G/H (at ±7°), and J/K (at ±15°). The latitudes of the J/K bands are just inside the latitudes of a nominal model

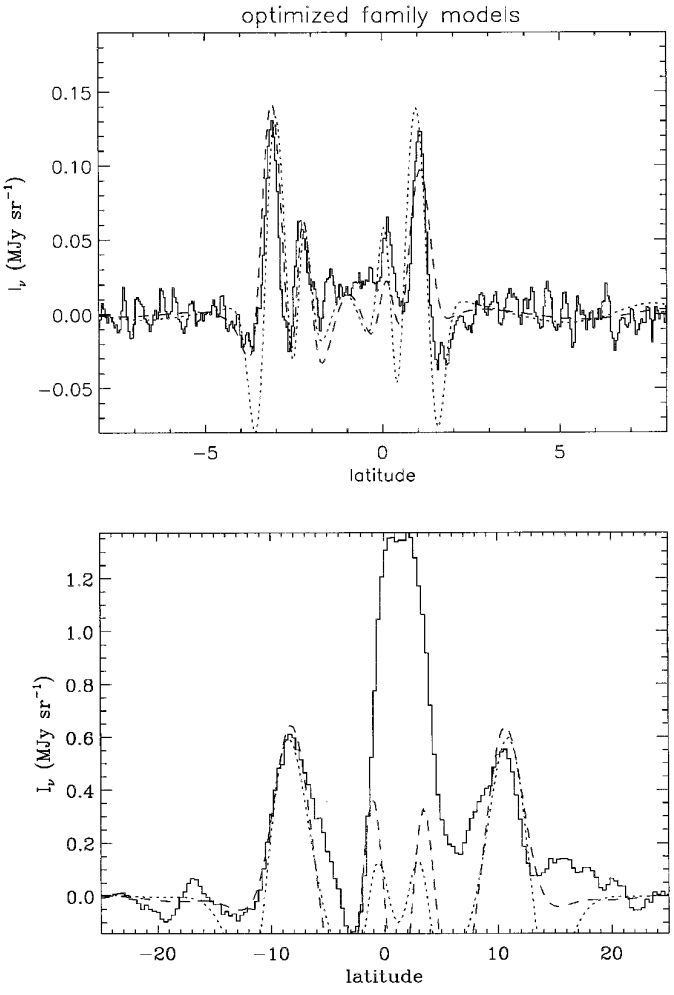

FIG. 14. Same as for Fig. 13, but for the optimized family models. The agreement of band latitudes is significantly better than for the nominal models, with the only change that the proper inclination of the dust is systematically lower than that of the parent asteroid family. Note also the good agreement between the shape of the observed brightness and the model, after both are processed with the same spatial filtering.

for the Eunomia family. Because the prominent bands also have latitudes smaller than those of the nominal family model, we consider the locations of the J/K bands to be in good agreement with the Eunomia family. Sykes (1988) tentatively associated the J/K pair with the Io family, which, as discussed above, is the same as the Eunomia family for our purposes. Based on our own coaddition of the DIRBE elongation-90 maps, we also find the J/K bands and some combination of the E/F or G/H bands. The J/K bands have a brightness around 0.1 MJy sr^{-1} after Fourier filtering. The density needed to make a Eunomia/Io family model match the observed brightness is listed in Table V.

The latitudes of the E/F and G/H bands are outside the Nysa and Flora families, so we consider such associations unlikely. Thus there remain two asteroid families with no dust bands (Nysa and Flora) and two dust bands with no known parent family (E/F and G/H). The upper limits to the volumetric cross sections of the Nysa and Flora families, obtained by dividing the upper limit to the brightness by the predicted brightness for a nominal volumetric cross section of 10^{-9} AU^{-1}, are shown in Table V, together with the full set of parameters to describe the models. It is noteworthy that both large families without identified dust bands are in the inner asteroid belt. The proximity to strong orbital resonances (which indeed shape the present distribution of asteroids themselves) may scramble the dust produced by the families, such that it does not reach the inner Solar System in a coherent dust band.

An important distinction between the asteroid family members and its dust should be recognized. The sharpness of the dust-band peaks is inversely related to the dispersion in the proper inclinations of the orbits. In our empirical model, the sharpness of the peaks is controlled by the parameter v_i, which was determined for each family using Eq. (4) and the dispersion in orbital elements of the asteroid family members. The asteroid families have a wide range of dispersions, some being compact and well defined (e.g., Maria) and others either diffuse or with multiple subfamilies (e.g., Flora). The peak volume density of a family scales approximately as $v_i^{-0.73}$. Between the most extreme cases of $v_i = 0.05$ (Maria) and $v_i = 0.55$ (Flora), there is a factor of 6 difference in the normalization of a model to the same observed brightness. Perhaps it is not a coincidence that the two large families that are the most dispersed are those that are not detected, while the somewhat smaller Maria family has a relatively sharp band. Not only is dust from a compact family more easily distinguished from the zodiacal cloud, but also the higher density of asteroids in a compact family means the collision rate (and thus the dust production rate) is higher. The upper limits for both Flora and Nysa are already conservative, as they were calculated with relatively large values of v_i. For other families, the model densities should be considered uncertain at the factor of two level.

We have exhausted our list of the seven largest families defined using the criteria listed above, but the E/F and G/H dust bands remain unattributed. Generalizing from the already established associations, we would expect the parent family to be populous and to have a relatively sharp proper inclination distribution. Further, as the large, inner-belt families (Nysa and Flora) have no known dust bands, we might suspect the family to be in the outer asteroid belt. As this work neared completion another substantial study of the population of asteroid families appeared (Zappalà *et al.* 1995), using a significantly expanded list of asteroids and two different, automated classification methods. The seven large families we considered in Table IV remain, with gener-

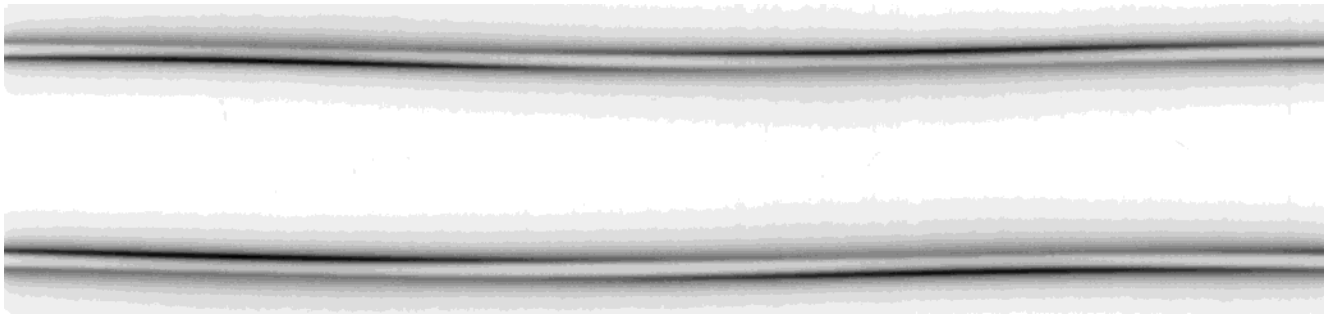

FIG. 15. Predicted surface brightness for the migrating model for the Koronis family, in a projection identical to the DIRBE elongation-90 maps. The "glints," where the northern or southern component of the dust band increases in brightness, occur when the Earth moves into the upper or lower edge of the emitting region, where the volume density of dust is highest.

ally increased populations. In addition, two other families appear to have very large membership in the new classification. They are in fact more populous than in the Maria family, which has a dust band, and therefore should be considered among potential dust-band parents. Both of these families are associated with very large asteroids—4 Vesta and 10 Hygiea—and are considered as possible cratering events (Zappalà *et al.* 1995). The proper inclination of these two families are such that they could well be the source of the E/F (Hygiea) and G/H (Vesta) dust bands. Their dispersion in proper inclinations is small enough that their dust bands would be relatively sharp, and neither family is located in the inner asteroid belt. If the association of dust bands with one or both of the Vesta and Hygiea families stands, then dust bands can be formed by two mechanisms: (1) catastrophic disruption of a large parent, with the subsequent comminution of the debris, and (2) cratering of a large asteroid in collisions with insufficient energy to disrupt it. We can further conclude that dust from one or both of these asteroids is present in the near-Earth environment, and some of the collected interplanetary dust particles may be pinpointed to one of these individual asteroids.

E. Total Surface Brightness of Dust Bands

Thus far we have considered only the spatial-filtered surface brightness of the dust bands, because this is their only clearly observable attribute; however, the dust bands contribute substantially more brightness than survives the median filtering. The dust distribution passes over and above the Earth's orbit, leading to a relatively smoothly varying surface brightness as a function of ecliptic latitude above the latitude of the dust-band peaks (Reach 1992). The total surface brightness at 25 μm, combining the migrating models of the detected dust bands, is shown as a function of ecliptic latitude in Fig. 16. The peak surface brightness (at 25-μm wavelength) of the model dust bands around 10° latitude is a full 10 MJy sr^{-1}, of which only 0.7 MJy sr^{-1} survives the Fourier filtering used for comparison with the observations in Fig. 8. For comparison, this amounts to some 12% of the zodiacal light brightness at this latitude and a typical solar elongation of 90°. The visible zodiacal light should have a comparable fractional contribution from the known dust bands, because the albedo of the dust bands is not much different from that of the particles in the remainder of the zodiacal cloud (Spiesman *et al.* 1995), and the line-of-sight weighting is similar for 25-μm surface brightness and scattered light.

F. Surface Area and Mass of Dust Bands

For those asteroid families with detected bands, we may estimate the total surface area for either the migrating or

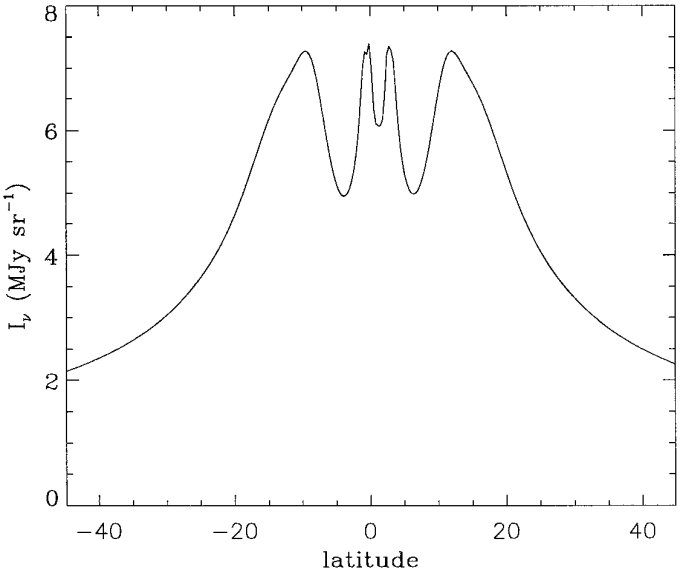

FIG. 16. The 25-μm surface brightness due to asteroid families as viewed from the Earth. The total of the migrating model surface brightnesses for each of the detected dust bands is shown as a function of ecliptic latitude for a line of sight 90° from the Sun. The brightness is dominated by the Koronis and Eos families, which have large populations and relatively sharp distributions of proper inclination.

torus model by integrating Eqs. (1) and (3), respectively. In terms of the empirical parameters, the total surface area of particles in a torus model is

$$A_{\rm tor} = \frac{\pi}{6} n_0 \delta_\zeta \delta_{\rm r} R_0^2 \left[\Gamma\left(\tfrac{1}{6}\right) + \frac{\Gamma\left(\frac{5}{6}\right)}{v_{\rm i}} \right] \left[\Gamma\left(\tfrac{1}{4}\right) + \frac{\Gamma\left(\frac{1}{4}\right)}{4 v_{\rm r}} + \frac{\sqrt{\pi}\delta_{\rm r}}{2 R_0 v_{\rm r}} + \sqrt{\pi}\frac{\delta_{\rm r}}{R_0} \right], \quad (5)$$

where n_0 is the absorption cross section per unit volume of dust-band particles at R_0. Similarly, for the migrating model,

$$A_{\rm mig} = \frac{\pi}{3} n_0 \delta_\zeta R_0^3 \left[\Gamma\left(\tfrac{1}{6}\right) + \frac{\Gamma\left(\frac{5}{6}\right)}{v_i} \right]. \quad (6)$$

Although it is not directly observed, it is perhaps easier to understand the total dust content of the dust bands through their total mass. The mass is clearly related to the total surface area, but it depends on the particle size: for spherical particles of single size, s, the mass density is $\langle nm \rangle = 4/3 \rho s n_0$ (as long as the particles are larger than the wavelength, $\lambda/2\pi$ at which the cross section was measured). For lack of an observed size distribution for the dust-band particles, we will use the Grün *et al.* (1985) size distribution of meteoroids near the Earth's orbit, for which

$$\langle nm \rangle = 1.24 \times 10^{-24} \left(\frac{n_0}{10^{-9}\ {\rm AU}^{-1}} \right) {\rm g\ cm}^{-3}.$$

For reference, this size distribution has a mass-weighted particle radius of 60 μm, and to first order the correction to a different effective particle size is linear. Using Eqs. (5) and (6) together with the values of n_0 and other parameters from Table V for the optimized family models, we calculated the surface areas and masses for the torus and migrating models for the Themis, Koronis, Eos, Eunomia/Io, and Maria families; the results are in Table VI. For families with no detected dust band (Nysa and Flora), an upper limit to the surface area was derived from the upper limit to n_0 from Table V and the parameters of a nominal dust band for that family. As discussed above, the values of n_0 are sensitive to the sharpness of the proper inclination distribution through the parameter $v_{\rm i}$; on the other hand, the masses are quite insensitive to $v_{\rm i}$.

For comparison, we also include the asteroid population for each family as derived from the two recent studies by Zappalá *et al.* (1994) and Williams (1992). The family population is contentious, because it cannot be guaranteed that the ranking of families according to the number of known asteroids is correct. Different definitions of families lead to very different population estimates. This applies especially to the Flora family, which is broken into several large subunits by Williams (1992) but considered as one large family by Zappalá *et al.* (1994). Further, there are obvious observational biases toward inner-belt and high-albedo asteroids, which are easier to see from the Earth, and perhaps even to the well-known and lower-inclination families because observers may spend more time tracking their orbits.

The dust-band mass is directly compared to the family population (from Williams 1992) in Fig. 17. The Flora family moves all the way to the bottom right part of this figure if it is considered as one large family rather than as

TABLE VI
Masses of Asteroidal Dust Bands

Family	$M_{\rm tor}$ (g)	$M_{\rm mig}$ (g)	$N_{\rm Zap}$[a]	$N_{\rm Will}$[b]
Themis	1.2×10^{16}	5.8×10^{15}	267	62
Koronis	3.4×10^{16}	3.7×10^{16}	147	42
Nysa	$<1 \times 10^{16}$	$<2 \times 10^{16}$	107	10
Flora	$<1 \times 10^{16}$	$<5 \times 10^{16}$	338	17[c]
Eos	6.7×10^{17}	3.2×10^{17}	220	74
Eunomia	$\sim 1 \times 10^{17}$	$\sim 1 \times 10^{17}$	100	22
Maria	$\sim 1 \times 10^{17}$	$\sim 2 \times 10^{17}$	38	14

[a] Number of members that are "numbered" asteroids from Zappalá *et al.* (1994).
[b] Number of members that are "numbered" asteroids from Williams (1992).
[c] Williams (1992) family 183 only.

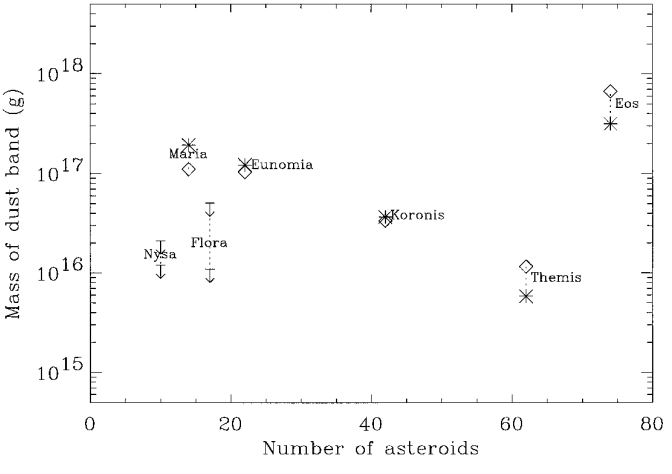

FIG. 17. Masses of the observed dust bands plotted as a function of the number of "numbered" asteroids in their associated families (Williams 1992). For each detected family, the mass calculated from the migrating (∗) and torus (◇) is shown as two symbols connected by a dotted line. Upper limits are shown for the Nysa and Flora families.

a group of subunits. While there is not a detailed one-to-one correlation between family population and dust-band mass, we can nonetheless gain some insight from these results. Sykes (1990) concluded that the lack of a one-to-one correspondence between dust bands and asteroid population indicates that the dust bands are intermittent, having been produced only by relatively recent collisional disruptions of individual asteroids. We suggest that the number of present-day dust bands is large enough, and the dynamic range of detected dust-band masses is small enough, that they should be considered relatively permanent features. Thus the lack of a dust band associated with a large family must be explained. The Eunomia/Io family evidently has a faint dust band, as discussed above, and its brightness is reasonable considering its population. If we believe the population estimates of Williams (1992), then Fig. 17 suggests that the lack of Flora and Nysa dust bands is not surprising. The fact that we do not see a prominent Flora dust band argues against a common origin for the very large Flora family (as found, e.g., by Zappalá *et al.* 1992).

V. DUST FROM NONFAMILY ASTEROIDS

While asteroid families produce appreciable amounts of dust and are detectable through the distinct signature of their dust bands, these dust bands explain only part of the observed brightness of the zodiacal light. Above, we estimated that detected dust bands produce some 12% of the brightness of the ecliptic. The associated asteroid families contain some 5% (Williams 1992) to 19% (Zappalá *et al.* 1994) of the population of numbered asteroids. Numbered asteroids are an observationally biased sample and are not necessarily a valid tracer of dust production: asteroid families are relatively less abundant in diameter-limited samples (Valsecchi *et al.* 1989). Nonetheless, it is plausible that nonfamily asteroids produce a significant fraction of the zodiacal light, as a simple scaling argument shows. Let us suppose that nonfamily asteroidal dust is distributed similar to the migrating dust-band model, but with such a wide range of inclinations that an edge-brightened dust band is not present:

$$n(r, \zeta) = n_0 \frac{R_0}{r} e^{-(\zeta/\delta_\zeta)^2}.$$

The width of the distribution can be directly obtained from the apparent distribution of asteroids; from the distribution of IRAS-detected asteroids (Veeder 1986), we find $\delta_\zeta \simeq 12°$. Adopting $R_0 = 3$ AU as we did for the dust bands, the mass of asteroidal dust is

$$M = 4 \times 10^{16} \left(\frac{n_0}{10^{-9}\,\mathrm{AU}^{-1}} \right) \mathrm{g}.$$

Also, the brightness through the center of this dust distribution, viewed from the Earth on a line of sight perpendicular to the Sun, is

$$I_\nu(0) \sim 0.3 \left(\frac{n_0}{10^{-9}\,\mathrm{AU}^{-1}} \right) \mathrm{MJy\ sr}^{-1}$$

at a wavelength of 25 μm.

The problem thus boils down to estimating the density of nonfamily asteroidal dust. A trivial upper limit may be placed by requiring that the surface brightness not exceed the observed brightness; for a brightness limit of 63 MJy sr^{-1} (the brightness of the ecliptic minus the contribution from known dust bands), the volumetric cross section must be $n_0 < 57 \times 10^{-9}$ AU^{-1}, and the mass must be $M_{\mathrm{nonfam}} < 8 \times 10^{18}$ g. For comparison, the total population of numbered asteroids is of order 4000. (We use numbered asteroids as a population tracer for lack of a better, unbiased tracer.) In order for nonfamily asteroids to account for all of the non-dust-band zodiacal light, the dust mass per nonfamily numbered asteroid would have to be

$$\frac{M}{N}(\mathrm{nonfamily}) \sim 2 \times 10^{15}\ \mathrm{g}.$$

For comparison, the dust bands have a dust mass per numbered asteroid in the range

$$9 \times 10^{13}\ \mathrm{g} < \frac{M}{N}(\mathrm{family}) < 1 \times 10^{16}\ \mathrm{g}$$

if we adopt the population estimates from Williams, or

$$2 \times 10^{13}\ \mathrm{g} < \frac{M}{N}(\mathrm{family}) < 5 \times 10^{15}\ \mathrm{g}$$

if we adopt the population estimates from Zappalá. Thus, if nonfamily asteroids produce dust at a rate that is similar to the dusty asteroid families, asteroidal dust could account for for the entire zodiacal light.

It is, however, likely that nonfamily asteroids produce less dust than family asteroids. Even known asteroid families exhibit a range of dust-band masses, and at least one prominent family (Nysa) lacks a detected dust band. Furthermore, asteroid families are not just concentrations of the asteroid populations at given orbital inclinations. Instead, they are concentrations in three dimensions of the phase space of orbital elements: semimajor axis, eccentricity, and inclination. Thus the collision rate among—and hence the dust production rate by—nonfamily asteroids is almost certainly lower than that of family asteroids. The

upper limit to the dust mass per numbered asteroid for the Nysa family is 2×10^{15} g (2×10^{14} g) for the Williams (Zappalá) population estimates. To produce all the zodiacal light, the nonfamily asteroids would have to produce 10 times as much dust per asteroid as the Nysa family if the larger family population is correct; however, in the case of the smaller (Williams) population estimate, it is still plausible that the asteroids do produce all the interplanetary dust responsible for the zodiacal light.

An independent estimate of the fraction of the interplanetary dust produced by asteroids has been made using the Earth's resonant dust ring (Jayaraman and Dermott 1996). By comparing the observed asymmetry of this ring to that expected for a population of dust particles with initially asteroidal orbits, it was found that between 10 and 100% of interplanetary dust is asteroidal. The result depends sensitively on the assumed size distribution of asteroidal particles, and is essentially the lower limit of 10%. We assign this lower limit to the nonfamily asteroids, because the asymmetry in the Earth's resonant ring is observed to be a smooth function of ecliptic latitude (Reach *et al.* 1995), rather than being similar to the dust-band distribution shown in Figs. 2 and 16. Applying this lower limit, we infer the mass of nonfamily asteroidal dust per nonfamily asteroid to be

$$\frac{M}{N}(\text{nonfamily}) > 3 \times 10^{14} \text{ g}.$$

Such a dust production rate is lower than that of asteroid families with detected dust bands, as expected, and is compatible with the upper limit placed on dust from the Nysa family.

VI. CONCLUSIONS

Based on our comparison of COBE/DIRBE and IRAS observations of the structure of the diffuse infrared sky brightness to empirical models for distribution of dust associated with the largest asteroid families, we conclude that the Themis, Koronis, Eos, Eunomia/Io, and Maria families produce substantial amounts of dust, while upper limits are placed on dust produced by the Nysa and Flora families, and two previously unattributed dust bands are suggested to be related to one or both of the Hygiea and Vesta families. The asteroid family orbital elements do not match those of the dust bands in detail. The radial distribution of dust is qualitatively different from that of the parent asteroids: the dust particles we observe now are significantly affected by Poynting–Robertson drag, so they are spread from the asteroid belt through the inner Solar System. Also, the vertical width of the dust distribution is larger than that of the parent asteroid families, with the same effect observed for each detected family. The enhanced width of the dust distribution probably reflects both the kinetic energy imparted to the dust when it is formed or dispersion by mutual collisions later on. The Nysa and Flora families may not produce easily discerned dust bands because the asteroids in the parent families are relatively widely dispersed in proper inclinations; alternatively, these families are no longer producing dust. Although the association between families and dust bands is not perfect, we conclude that dust bands are commonly associated with asteroid families. Thus it is likely that dust has been produced in asteroid families ever since the original events that formed them. Nonfamily asteroids may produce more dust than the asteroid families, because there are more of them, but estimates of the abundance of nonfamily asteroidal dust are still uncertain by at least an order of magnitude.

ACKNOWLEDGMENTS

W.T.R. thanks Andrea Milani for providing the table of proper elements of the asteroids, Jean-Philippe Bernard for helping with map projections, Mark Sykes and Stan Dermott for valuable discussions, Mike Hauser for extensive comments in the early phases of this project, Dan Durda and Michael Rowan-Robinson for helping him focus on the big picture with their referee's reports. This work made extensive use of the COBE Guest Investigator Software (CGIS) package that was developed at the Cosmology Data Analysis Center.

REFERENCES

Boggess, N. W., J. C. Mather, R. Weiss, C. L. Bennett, E. S. Cheng, E. Dwek, S. Gulkis, M. G. Hauser, M. A. Janssen, T. Kelsall, S. S. Meyer, S. H. Moseley, T. L. Murdock, R. A. Shafer, R. F. Silverberg, G. F. Smoot, D. T. Wilkinson, and E. L. Wright 1992. The COBE mission: Its design and performance two years after launch. *Astrophys. J.* **397,** 420–429.

Burns, J. A., P. L. Lamy, and S. Soter 1979. Radiation forces on small particles in the Solar System. *Icarus* **40,** 1–48.

Carusi, A., and G. B. Valsecchi 1992. On asteroid classifications in families. *Astron. Astrophys.* **115,** 327–335.

Chapman, C. R., V. Paolocchi, R. P. Zappalà, and J. F. Bell 1989. Asteroid families: Physical properties and evolution. In *Asteroids II* (R. P. Binzel, T. Gehrels, and M. S. Matthews, Eds.), pp. 386–415. Kluwer, Dordrecht.

Davies, J. K., S. F. Green, A. J. Meadows, B. C. Stewart, and H. H. Aumann 1984. The IRAS fast-moving object search. *Nature* **309,** 315–319.

Dermott, S. F., D. D. Durda, B. Å. S. Gustafson, S. Jayaraman, J. C. Liou, and Y. L. Xu 1994a. Zodiacal dust bands. In *Asteroids, Comets, and Meteors 1993, Proceedings of IAU Symposium 160* (A. Milani, M. DiMartino, and A. Cellino, Eds.), pp. 127–142. Kluwer, Boston.

Dermott, S. F., S. Jayaraman, Y. L. Xu, K. Grogan, and B. Å. S. Gustafson 1996. The origin and dynamics of the interplanetary dust cloud. In *Unveiling the Cosmic Infrared Background* (E. Dwek, Ed.), pp. 25–36. AIP, New York.

Dermott, S. F., S. Jayaraman, Y. L. Xu, B. Å. S. Gustafson, and J. C.

Liou 1994b. A circumsolar ring of asteroidal dust in resonant lock with the Earth. *Nature* **369,** 719–723.

Dermott, S. F., P. D. Nicholson, J. A. Burns, and J. R. Houck 1984. Origin of Solar System dust bands discovered by IRAS. *Nature* **312,** 505–509.

Dermott, S. F., P. D. Nicholson, J. A. Burns, and J. R. Houck 1985. An analysis of IRAS' Solar System dust bands. In *Properties and Interactions of Interplanetary Dust* (R. H. Giese and P. Lamy, Eds.), pp. 395–409. Reidel, Dordrecht.

Dermott, S. F., P. D. Nicholson, Y. Kim, B. Wolven, and E. F. Tedesco 1988. The impact of IRAS on Asteroidal Science. In *Comets to Cosmology* (A. Lawrence, Ed.), pp. 3–18. Springer-Verlag, Berlin.

Good, J. C. 1994. Zodiacal dust cloud modeling using IRAS data. In *IRAS Sky Survey Atlas: Explanatory Supplement* (S. L. Wheelock, T. N. Gautier, J. Chillemi, D. Kester, H. McCallon, C. Oken, J. White, D. Gregorich, F. Boulanger, and J. Good, Eds.), pp. G1–G14. Publication 94-11, JPL, Pasadena, CA.

Grün, E., M. Baguhl, N. Divine, H. Fechtig, D. P. Hamilton, M. S. Hanner, J. Kissel, B.-A. Lindblad, D. Linkert, G. Linkert, I. Mann, J. A. M. McDonnell, G. E. Morfill, C. Polanskey, R. Riemann, G. Schwehm, N. Siddique, P. Staubach, and H. A. Zook 1995a. Three years of Galileo dust data. *Planet. Space Sci.* **43,** 953–969.

Grün, E., M. Baguhl, N. Divine, H. Fechtig, D. P. Hamilton, M. S. Hanner, J. Kissel, B.-A. Lindblad, D. Linkert, G. Linkert, I. Mann, J. A. M. McDonnell, G. E. Morfill, C. Polanskey, R. Riemann, G. Schwehm, N. Siddique, P. Staubach, and H. A. Zook 1995b. Two years of Ulysses dust data. *Planet. Space Sci.* **43,** 971–999.

Grün, E., H. A. Zook, H. Fechtig, and R. H. Giese 1985. Collisional balance of the meteoritic complex. *Icarus* **62,** 244–272.

Hanner, M. S., and J. L. Weinberg 1974. Changes in zodiacal light with heliocentric distance: Preliminary results from Pioneer 10. *Space Res.* **14,** 769–772.

Hauser, M. G. 1996. Searching for the cosmic infrared background. In *Unveiling the Cosmic Infrared Background* (E. Dwek, Ed.), pp. 11–21. AIP, New York.

Hauser, M. G., F. C. Gillett, F. J. Low, T. N. Gautier, C. A. Beichman, H. H. Aumann, G. Neugebauer, B. Baud, N. Boggess, and J. P. Emerson 1984. IRAS observations of the diffuse infrared background. *Astrophys. J.* **278,** L15–L18.

Hirayama, K. 1918. Groups of asteroids probably of common origin. *Astron. J.* **31,** 185–743.

Hong, S. S. 1985. Henyey–Greenstein representation of the mean volume scattering phase function for zodiacal dust. *Astron. Astrophys.* **146,** 67–75.

Jackson, A. A., and H. A. Zook 1989. A Solar System dust ring with the Earth as its shepherd. *Nature* **337,** 629–631.

Jayaraman, S., and Dermott, S. F. 1996. Estimating the asteroidal component of the zodiacal cloud using the Earth's resonant ring. In *Physics, Chemistry, and Dynamics of Interplanetary Dust* (B. A. S. Gustafson and M. S. Hanner, Eds.), pp. 155–158. ASP, San Francisco.

Jones, M. H., and M. Rowan-Robinson 1993. A physical model for the IRAS zodiacal dust bands. *Mon. Not. R. Astron. Soc.* **264,** 237–247.

Leinert, C., I. Richter, E. Pitz, and N. Planck 1981. The zodiacal light from 1.0 to 0.3 AU as observed by the Helios space probes. *Astron. Astrophys.* **103,** 177–188.

Love, S. G., and D. E. Brownlee 1992. The IRAS dust band contribution to the interplanetary dust complex: Evidence seen at 60 and 100 μm. *Astron. J.* **104,** 2236–2242.

Low, F. J., E. Young, D. A. Beintema, T. N. Gautier, C. A. Beichman, H. H. Aumann, F. C. Gillett, G. Neugebauer, N. Boggess, and J. P. Emerson 1984. Infrared cirrus: New components of the extended infrared emission. *Astrophys. J.* **278,** L19–L22.

Marzari, F., D. Davis, and V. Vanzani 1995. Collisional evolution of asteroid families. *Icarus* **113,** 168–187.

Milani, A., and Z. Knežević 1990. Secular perturbation theory and computation of asteroid proper elements. *Celest. Mech.* **49,** 247–411.

Reach, W. T. 1988. Zodiacal emission. I. Dust near the Earth's orbit. *Astrophys. J.* **335,** 468–485.

Reach, W. T. 1991. Zodiacal emission. II. Dust near the Ecliptic. *Astrophys. J.* **369,** 529–543.

Reach, W. T. 1992. Zodiacal emission. III. Dust near the asteroid belt. *Astrophys. J.* **392,** 289–299.

Reach, W. T., A. Abergel, F. Boulanger, F.-X. Desert, M. Perault, J.-P. Bernard, J. Blommaert, C. J. Cesarsky, D. Cesarsky, L. Metcalfe, J.-L. Puget, F. Sibille, and L. Vigroux 1996a. Mid-infrared spectrum of the zodiacal light. *Astron. Astrophys.* **315,** L381–L384.

Reach, W. T., B. A. Franz, T. Kelsall, and J. L. Weiland 1996b. DIRBE observations of the zodiacal light. In *Unveiling the Cosmic Infrared Background* (E. Dwek, Ed.), pp. 37–46. AIP, New York.

Reach, W. T., B. A. Franz, J. L. Weiland, M. G. Hauser, T. N. Kelsall, and G. Rawley 1995. Observational confirmation of a circumsolar dust ring by the COBE satellite. *Nature* **374,** 521–523.

Spiesman, W. J., M. G. Hauser, T. Kelsall, C. M. Lisse, S. H. Moseley, Jr., W. T., Reach, R. F. Silverberg, S. W. Stemwedel, and J. L. Weiland 1995. Near and far infrared observations of interplanetary dust bands from the COBE Diffuse Infrared Background Experiment. *Astrophys. J.* **442,** 662–667.

Sykes, M. V. 1988. IRAS observations of extended zodiacal structures. *Astrophys. J.* **334,** L55–L58.

Sykes, M. V. 1990. Zodiacal dust bands: Their relation to asteroid families. *Icarus* **84,** 267–289.

Sykes, M. V., and R. Greenberg 1986. The formation and origin of the IRAS zodiacal dust bands as a consequence of single collisions between asteroids. *Icarus* **65,** 51–69.

Sykes, M. V., R. Greenberg, S. F. Dermott, P. D. Nicholson, J. A. Burns, and T. N. Gautier 1989. Dust bands in the asteroid belt. In *Asteroids II* (R. P. Binzel, T. Gehrels, and M. S. Matthews, Eds.), pp. 336–367. Univ. of Arizona Press, Tucson.

Sykes, M. V., L. A. Lebofsky, D. M. Hunten, and F. J. Low 1986. The discovery of dust trails in the orbits of periodic comets. *Science* **232,** 1115–1117.

Sykes, M. V., and R. G. Walker 1992. Cometary dust trails. I. Survey. *Icarus* **95,** 180–210.

Valsecchi, G. B., A. Carusi, Z. Knežević, L. Kresák, and J. G. Williams 1989. Identification of asteroid dynamical families. In *Asteroids II* (R. P. Binzel, T. Gehrels, and M. S. Matthews, Eds.), pp. 368–385. Univ. of Arizona Press, Tucson.

Veeder, G. J. 1986. The IRAS asteroid data. In *Infrared Astronomical Satellite Asteroid and Comet Survey* (D. L. Matson, Ed.), pp. 2.1–2.54. JPL, Pasadena, CA.

Wainscoat, R. J., M. Cohen, K. Volk, H. J. Walker, and D. E. Schwartz 1992. A model of the 8–25 micron point source infrared sky. *Astrophys. J. Suppl.* **83,** 111–146.

Weiland, J. L., R. G. Arendt, and T. J. Sodroski 1996. The interstellar dust contribution to the diffuse infrared sky brightness. In *Unveiling the Cosmic Infrared Background* (E. Dwek, Ed.), pp. 74–86. AIP, New York.

Wheelock, S. L., T. N. Gautier, J. Chillemi, D. Kester, H. McCallon, C. Oken, J. White, D. Gregorich, F. Boulanger, and J. Good 1994. *IRAS Sky Survey Atlas: Explanatory Supplement.* JPL, Pasadena, CA.

Williams, J. G. 1992. Asteroid families: An initial search. *Icarus* **96,** 251–280.

Wyatt, S. P., and F. L. Whipple 1950. The Poynting–Robertson effect on meteor orbits. *Astrophys. J.* **111,** 134–141.

Zappalà, V., Ph. Bendjoya, A. Cellino, P. Farinella, and C. Froeschlé 1995. Asteroid families: Search of a 12,487-asteroid sample using two different clustering techniques. *Icarus* **116,** 291–314.

Zappalà, V., A. Cellino, P. Farinella, and Z. Knežević 1990. Asteroid families. I. Identification by hierarchical clustering and reliability assessment. *Astron. J.* **100,** 2030–2046.

Zappalà, V., A. Cellino, P. Farinella, and A. Milani 1994. Asteroid families. II. Extension to unnumbered multiopposition asteroids. *Astron. J.* **107,** 772–801.